Journal of Radioanalytical and Nuclear Chemistry (2020) 323:515–537
https://doi.org/10.1007/s10967-019-06953-4

Manganese ferrite ($MnFe_2O_4$) as potential nanosorbent for adsorption of uranium(VI) and thorium(IV)

Marwa Alaqarbeh[1,3] · Fawwaz I. Khalili[1] · Olfa Kanoun[2]

Received: 5 September 2019 / Published online: 2 December 2019

Abstract
The adsorption behavior of U(VI) and Th(IV) metal ions by $MnFe_2O_4$ NPs was studied as a function of pH, mass of sorbent, contact time, and temperature. Kinetic data was fitted to Pseudo second-order model and q_m reached maximum value at pH 3 for Th(IV) and at pH 3.0–5.0 for U(VI) after 3 h. The Langmuir, Freundlich, and Dubinin–Raduskevich isotherm equations were applied to the adsorption data and the proper constants were derived. Adsorption isotherms were studied at different temperature to find $\Delta H°$, $\Delta G°$, and $\Delta S°$. Recovery was carried out by using 0.10 M of HNO_3, HCl, EDTA, Na_2CO_3 and NaCl.

Keywords Adsorption · Manganese ferrite · Magnetic nanosorbent · U(VI) · Th(IV)

Introduction

The adsorption method is one of the green methods for water purification, because it is a reversible process, simply operated, most applied and cost-effective method to get rid of the different water pollutants [1]. The mechanism of adsorption process depends on adhesion of the adsorbate at the surface of the sorbent. It is controlled by several conditions: medium pH, concentration of adsorbate, time of adsorbate coverage, and surface area to pore volume size of sorbent [2, 3].

Different natural and synthetic sorbents are used for pollutants removal; natural sorbents are preferred rather than synthetic sorbents, due to their low cost, ease of production, and being environmentally friendly. The sorbent is preferred to contain a hydroxyl group, amine, phosphorus, or sulfur atoms to chelate heavy metal pollutants [4–6].

The sorbents used are: activated carbon [7], bentonite [8], and zeolite [8–10], humic acid [11], chitosan [12], organic biomass [13], clays [14], red mud [15], sludge [16], and fruit peels such as orange and lemon peels [17].

Recently new materials in nanoscale, where the size measured in $(1–100)\times10^{-9}$ m were used. They have unique properties such as: large surface area, high surface activity, easily fabricated, reusable, and high specificity [18–23]. Carbonaceous nanomaterials (CNMs) such as: carbon nanoparticles (CNPs), carbon nanosheets (CNSs) [24–26]. Silicon nanomaterials (SiNMs) include silicon nanotubes (SiNTs), silicon nanoparticles (SiNPs), and silicon nanosheets [26]. Zero-valent transition metals and metal oxide NPs, iron-based nanosorbents such as iron oxides, oxyhydroxides and hydroxides, including ferric oxide/hydroxide as goethite (α-FeOOH) [27–30], and iron oxide hematite (α-Fe_2O_3) [31], maghemite (γ-Fe_2O_3), magnetite (Fe_3O_4) [32], and spinel metal iron(III) oxide $M^{n+}(Fe_3O_4)$, (M = Mn, Zn, Co, Mg, and Ni) [32, 33]. They are the most widely used nanomaterials for water treatment because they have a higher adsorption capacity and a faster adsorption rate in comparison with other sorbents. In addition, magnetic properties facilitate their separation from liquid media by magnet [33–36].

$MnFe_2O_4$ NPs "jacobsite" belong to spinel structure of metal oxides, with general chemical formula $A^{2+}O\ A_2{}^{3+}O_3$ where A^{2+} = Mg, Mn, Fe, Co, Ni, Cu, Zn and A^{3+} = Al, V, Cr, Mn, Fe, Co [37–39]. Several fabrication methods have been used to fabricate $MnFe_2O_4$ NPs such as: sol–gel [40, 41], chemical co-precipitation method [42, 43], auto-combustion and thermal decomposition [44–46], ball mechanical milling [47], reverse micelle synthesis [48], and pulsed laser

✉ Marwa Alaqarbeh
marwaqarbh@hotmail.com; marwa.alaqarbeh@narc.gov.jo

[1] Department of Chemistry, School of Science, The University of Jordan, Amman 11942, Jordan

[2] Department of Electrical Engineering and Information Technology, Technische Universität Chemnitz, Str. der Nationen 62, 09111 Chemnitz, Germany

[3] Present Address: National Agricultural Research Center, Al-Baqa 19381, Jordan

deposition [49]. $MnFe_2O_4$ NPs used diverse applications in different fields such as: magnetic resonance imaging (MRI), biotechnology, medical diagnostics and drug delivery [50, 51], storage devices and sensors [52, 53], catalysis [54, 55], and environmental applications as sorbent and electrodeposition electrode [56–58]. The aim of this work is to fabricate $MnFe_2O_4$ NPs and to use it as a sorbent for removal of U(VI) and Th(IV) ions from aqueous solutions, due to its high chemical and thermal stability at different chemical and thermal conditions. In addition to its magnetic properties facilitate their separation from liquid media by magnet.

Materials and methods

Material

All reagents used in this research were analytical grade reagents, with no further purification. Sodium hydroxide pellets (NaOH) from SDS vorte partenaire chimie, hydrochloric acid 37% (HCl) from S&C Chemical Supplico, nitric acid 69% (HNO_3) and ferric(III) chloride hexahydrate ($FeCl_3{\cdot}6H_2O$) from LAB CHEM, sodium carbonate (Na_2CO_3), polyvinylpyrrolidone (PVP), EDTA from BDH PROLABO, sodium chloride (NaCl) from GAINLAND CHEMICAL COMPANY (GCC), manganese(II) chloride tetrahydrate ($MnCl_2{\cdot}4H_2O$) from MERK, potassium hydrogen phthalate (KHP), thorium(IV) nitrate tetrahydrate ($Th(NO_3)_4{\cdot}4H_2O$), and uranyl(VI) nitrate hexahydrate ($UO_2(NO_3)_2{\cdot}6H_2O$) from BDH Chemicals Ltd Poole England, Arsenazo(III) indicator from JANSSEN CHIMICA, $MnFe_2O_4$ nanopowder/nanoparticles with 99.99%, of 28 nm from US Research Nanomaterials, Inc., absolute ethanol, and acetone from SELVO CHEM and 99.5% glacial acetic acid from TEDIA.

Instruments

Weighing was done by RADWAG®AS 220. R2 Electronic Balance. The pH of the solutions was measured with a EUTECH pH-meter. Fourier-transform infrared spectroscopy (FT-IR) spectra was measured by using Thermo Nicolet NEXUS 670 FT–IR Spectrophotometer. Thermal gravimetric analysis (TGA) was carried by using NETZCH STA 409 PG/PC, thermal analyzer in the temperature range (25–1000 °C) at heating rate of 20 °C/min. Thermal stability and melting point were carried by NETZCH differential scanning calorimeter (DSC) 204 F1, calorimetric analysis in the temperature range (20–500 °C) at heating rate of 10 °C/min. X-ray diffraction (XRD) was measured by using Philips X pert PW 3060, operated at 45 kV and 40 mA. The shape with 3-dimension (3D) surface morphology and energy dispersion spectrum (EDXS) to determine point elemental composition was examined with NCFL's FEI QUANTA 600 FEG scanning electron microscope (SEM). The nature of the surface and average size was carried by magneton MORGAGNI FEI 500 tunneling electron microscopy. Samples were shaken by using GFL-1083 thermostatic shaker. The material was calcinated by using NEBER Industrieofenbeu 2804 Lilinthal/Bremen furnace and dried by using nuve FN 500 oven. The concentrations of the metal ions were determined by using Vis Spectrophotometer from METASH model V-5100, and a 1.0 cm quartz cell. Material was grinded by mini Philips milling machine, zeta potential was measured using Zetasizer Nano ZS90 (Malvern Instruments).

Fabrication of manganese iron oxide $MnFe_2O_4$ NPs

By using previous procedures, $MnFe_2O_4$ NPs was fabricated by two methods, chemical co-precipitation method [44] and thermal treatment method [33, 45]. A modified chemical co-precipitation method was used by using 0.01 mol ($MnCl_2{\cdot}4H_2O$) and 0.02 mol ($FeCl_3{\cdot}6H_2O$) dissolved in 100.0 mL of DI water under vigorous stirring at 1200 rmp. The pH was slowly raised to 12.0 by adding 5.0 M NaOH solution dropwise. The reaction mixture was refluxed at 95–100 °C for 24 h, then it was stopped, cooled, and the magnetic product was separated by neodymium magnet. Finally, it was washed with distilled water, ethanol, and acetone, and it was dried at 120 °C for 48 h and then grinded by mini Philips machine.

Adsorption and desorption experiments

Standard solutions of ($UO_2(NO_3)_2{\cdot}6H_2O$) and ($Th(NO_3)_4{\cdot}4H_2O$) of different concentrations ranging from 10 to 100 ppm were used, the pH of standard solution was adjusted by using (KHP)/(HCl) or KHP/NaOH as a buffer solution to adjust the solutions pH to 1.0, 2.0, 5.0, 6.0, and 7.0, whereas pH at 3.0 and 4.0 was adjusted by NaCl/HCl buffer solution.

Adsorption studies for metal ions were obtained by performing batch techniques at 25 °C using purchased $MnFe_2O_4$ NPs as mentioned in "Material" section. In order to optimize the equilibrium conditions: mass of sorbent, pH of solution, initial metal concentration, and contact time, a 5.00 mL of 50 ppm of metal ions solution was used with some certain amounts of $MnFe_2O_4$ NPs ranging from 1.000 to 5.000 mg. After that, the optimized mass sorbent was used with 5.00 mL of 50 ppm of metal ions solution with different pH range (1.0–7.0) to optimize pH solution. The samples with 5.00 mL of 50 ppm of metal ions solution of optimized pH were exposed to constant shaking time for 12 h to reach equilibrium conditions', sampling was performed by taking aliquots at predetermined time intervals (every 30 min).

(A) FT-IR spectrum.

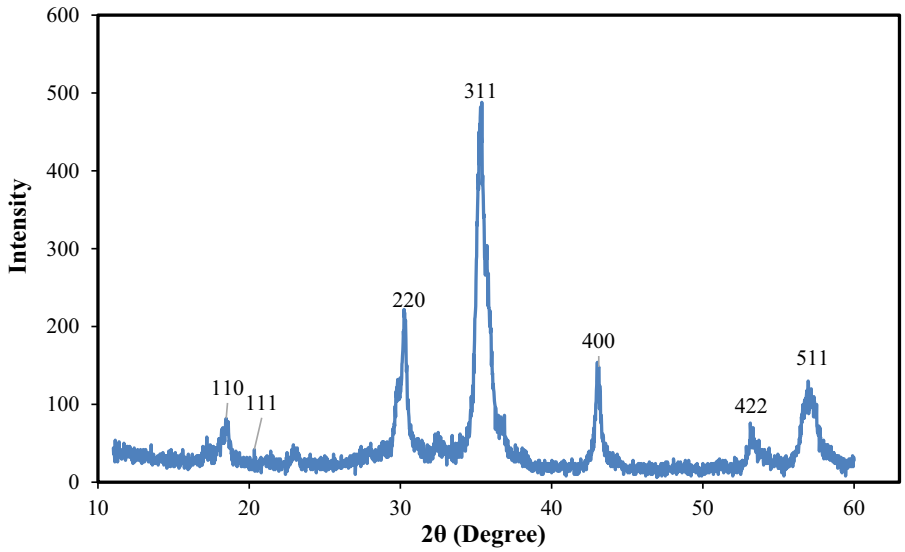

(B) XRD for $MnFe_2O_4$.

Fig. 1 **a** FT-IR spectrum, **b** XRD, **c** TGA, **d** DSC for $MnFe_2O_4$

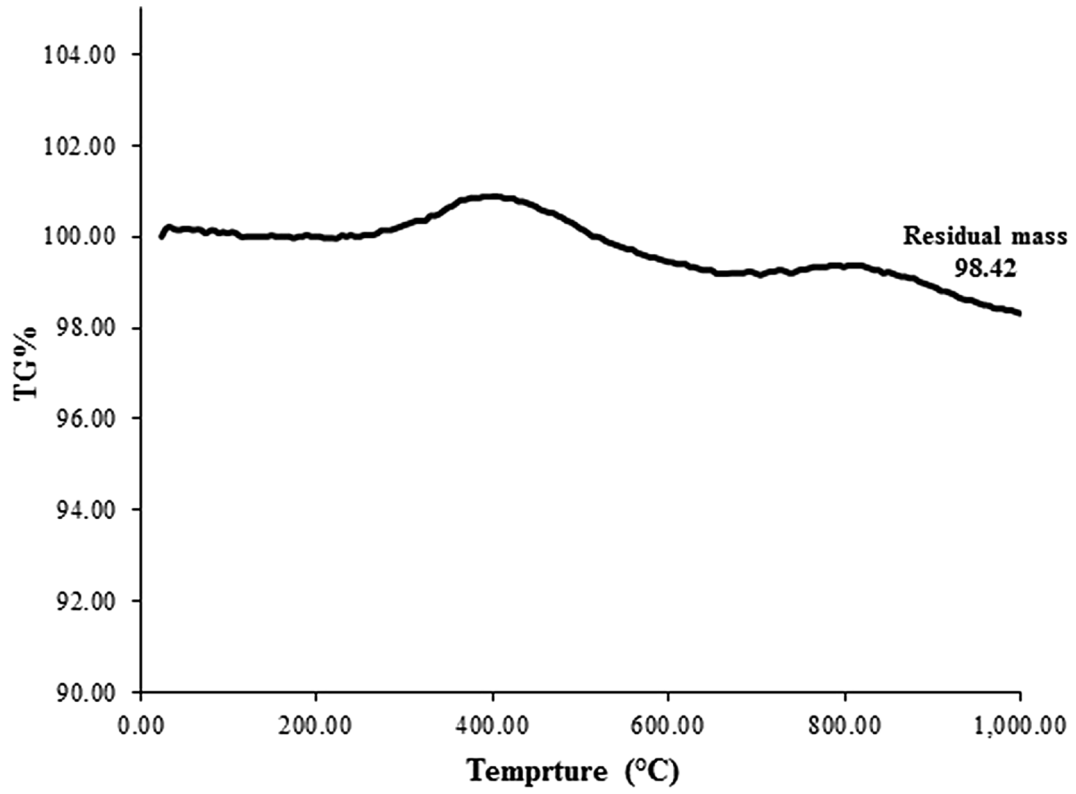

(C) TGA for $MnFe_2O_4$.

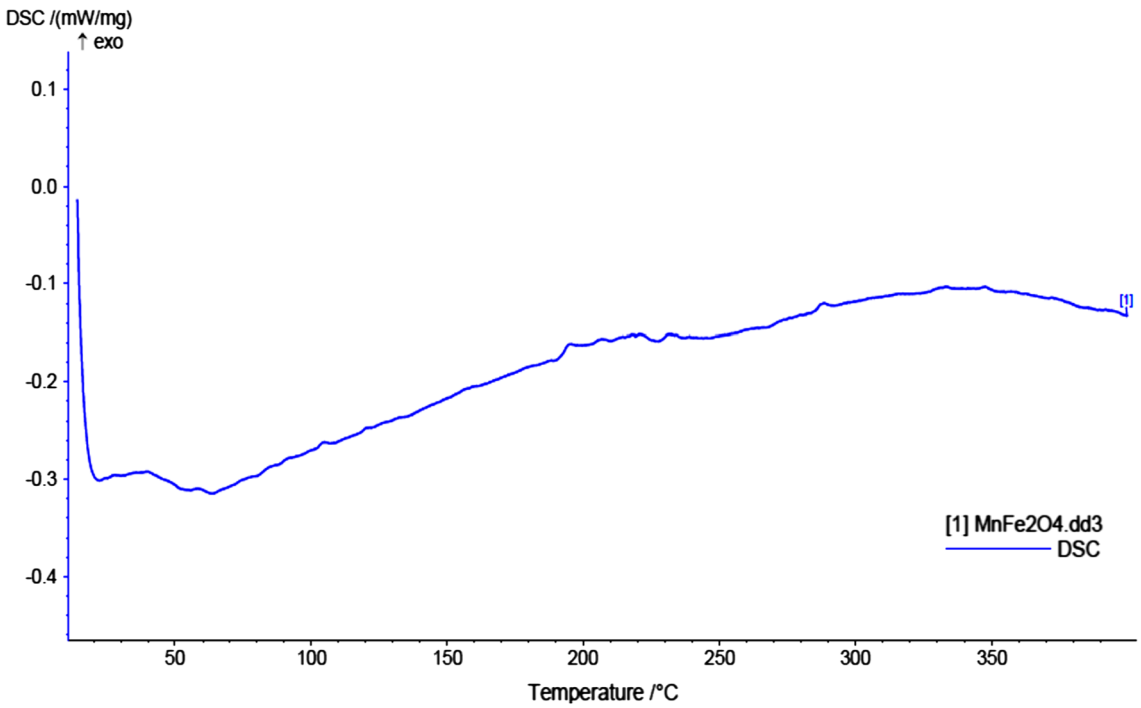

(D) DSC for $MnFe_2O_4$.

Fig. 1 (continued)

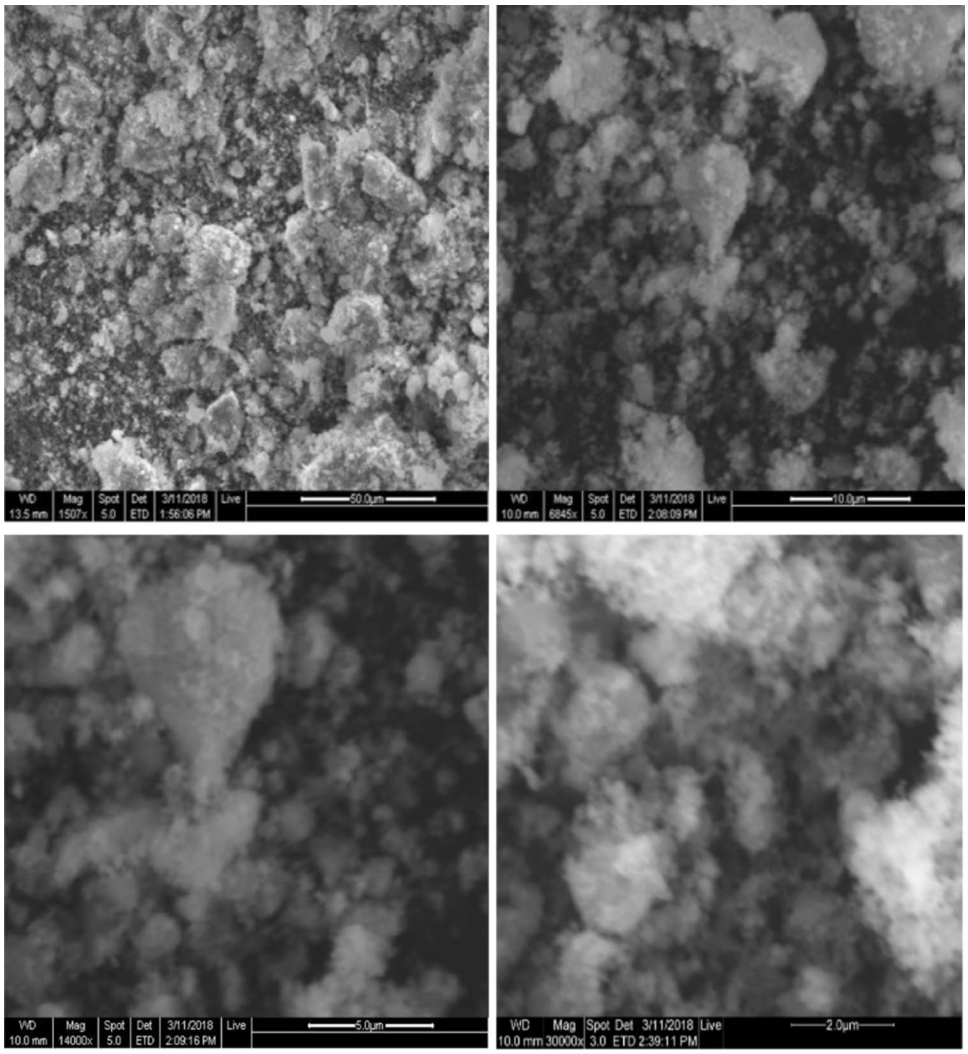

(A) SEM for $MnFe_2O_4$ NPs.

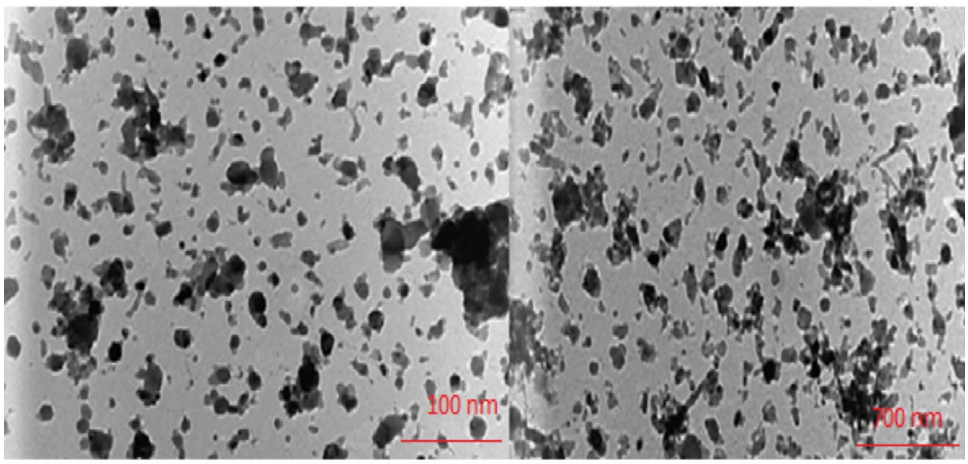

(B) TEM for $MnFe_2O_4$ NPs.

Fig. 2 **a** SEM, **b** TEM for $MnFe_2O_4$ NPs

Table 1 Size distribution of $MnFe_2O_4$ particles

Samples	Area $(nm)^2$	Length (nm)
1	9.04	13.20
2	8.63	12.63
3	9.86	15.01
4	8.63	12.82
5	4.11	5.73
6	11.10	16.67
Average	8.56	12.68

The adsorption data were fitted to the following isotherm models Langmuir, Freundlich, and D–R models. The adsorption capacity q_e (mg/g) (equilibrium amount of adsorbate adsorbed per unit mass of sorbent) was calculated from Eq. (1) and removal yield was calculated from Eq. (2):

$$q_e = \left(C_o - C_e\right)\frac{V}{m} \tag{1}$$

$$\%\,P = \frac{\left(C_o - C_e\right)}{C_o} \times 100 \tag{2}$$

where C_e is the equilibrium concentration of adsorbate (mg/L), C_o is the initial concentration of adsorbate in the bulk (mg/L), V is the solution volume (L), and m is sorbent mass (mg).

Desorption of metal ions from $MnFe_2O_4$ NPs surfaces was investigated by using batch techniques. It was started by loading of metal ions onto $MnFe_2O_4$ NPs, and then was leached through 5 cycles with different time intervals, using five eluents HNO_3, NaCl, Na_2CO_3, HCl, and EDTA with 0.10 M concentration, the desorption recovery yield was calculated from Eq. (3):

$$\%\,R = \frac{\left(C_{ads} - C_{des}\right)}{C_{ads}} \times 100\% \tag{3}$$

Determination of U(VI) and Th(IV)

The concentration of metal ions was measured by Vis absorption spectroscopy, using 0.1% Arsenazo(III) indicator as a colorimetric agent. 0.50 mL of 0.1% Arsenazo(III) indicator was added to 1.0 mL of the aqueous test, and 10.00 mL of 9.0 M hydrochloric acid solution for Th(IV) solution or of 0.01 M hydrochloric acid solution for U(IV) solution in 25 mL volumetric flask, the volume was completed to mark with deionized water and was shacked well. Absorbance measurements were carried out by using a 1.0 cm quartz cell within 1 h of sample preparation at 660 nm to detect Th(IV) ions, and 650 nm to detect U(VI) ions since each metal ion was studied separately [59, 60].

Table 2 EDXS chemical elements composition of $MnFe_2O_4$, $MnFe_2O_4$/U(VI) and $MnFe_2O_4$/Th(IV)

Materials	C Kα	O Kα	Mn Kα	Fe Kα	U Kα	Th Kα
$MnFe_2O_4$	–	6.97	26.93	66.10	–	–
$MnFe_2O_4$/U(VI)	6.33	13.58	23.29	55.93	0.21	–
$MnFe_2O_4$/Th(IV)	1.22	3.9	27.84	66.23	–	0.76

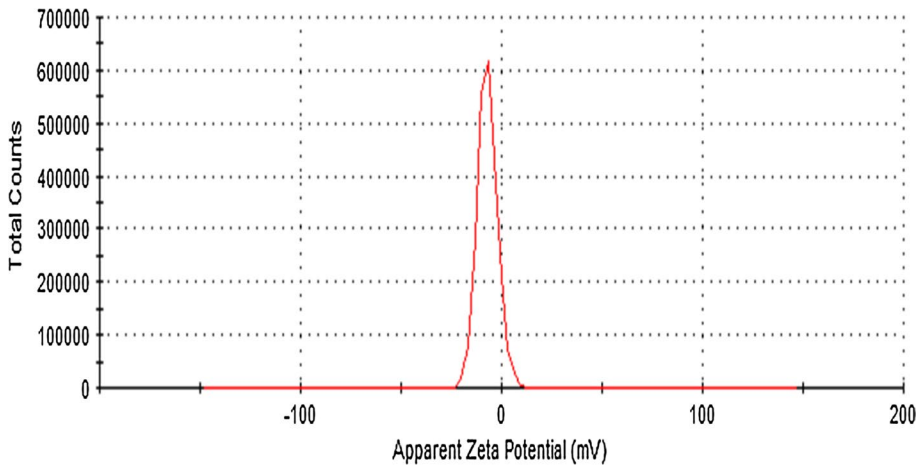

Fig. 3 Zeta potential distribution

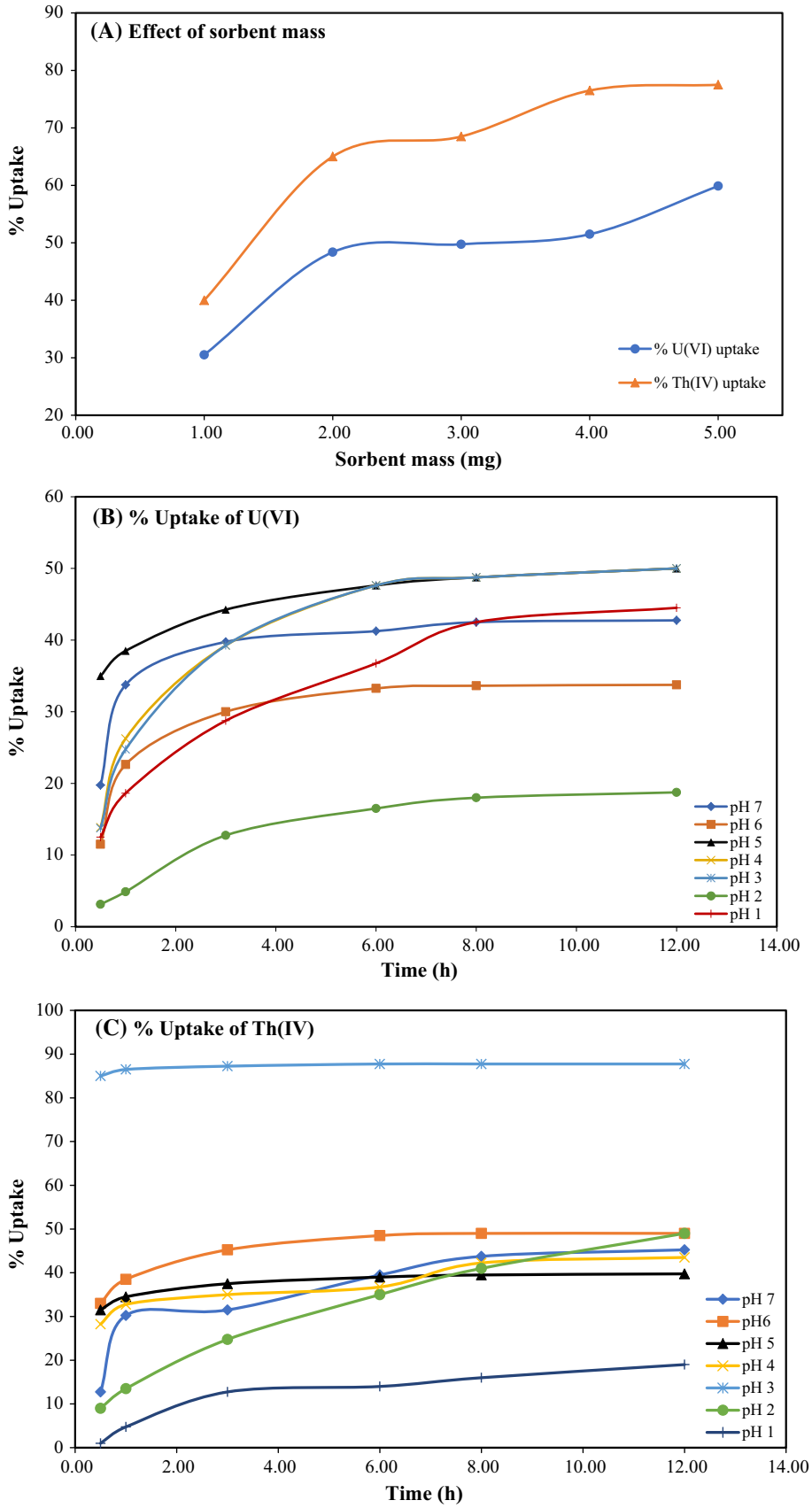

Fig. 4 **a** Effect of $MnFe_2O_4$ NPs mass for 50 ppm U(VI) and Th(IV), $t = 12$ h, pH 3.0, at 25.0 °C. **b** % Uptake of U(VI) by at different pH. **c** % Uptake of Th(IV) at different pH. **d** Effect of metal ion concentration. **e** Effect of contact time of adsorption metal ions by $MnFe_2O_4$ NPs at 25.0 °C

Fig. 4 (continued)

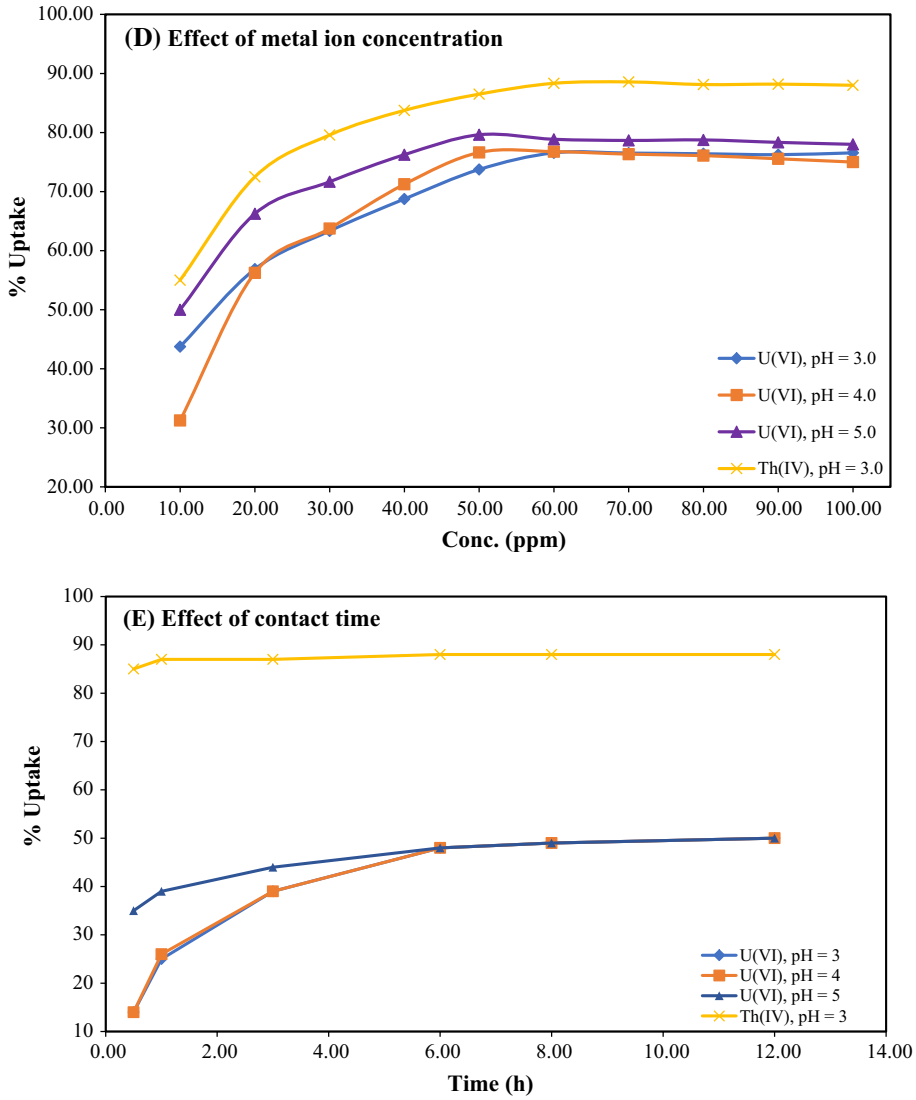

Results and discussion

Characterization of $MnFe_2O_4$

Figure 1a shows the FT-IR spectrum of $MnFe_2O_4$, it includes a stretching band at 568.4 cm^{-1} for (Fe–O) and 649.6 cm^{-1} for (Mn–O) which represents the spinel structure of iron [61–63]. The diffractogram of $MnFe_2O_4$ NPs given in Fig. 1b shows diffraction peaks at 18.66° (110), 20.56° (111), 30.32° (220), 35.38° (311), 43.12° (400), 52.12° (422), and 57.12° (511), which are the characteristic peaks of $MnFe_2O_4$ NPs having an inverse cubic spinel structure (cubic, space group: *Fd3 m*) and agrees with $MnFe_2O_4$ NPs which were previously fabricated [33]. The particle size can be quantitatively evaluated from the XRD data by using the Debye–Scherrer Eq. (4), which gives a relationship between peak broadening in XRD and particle size.

$$D = \frac{k\lambda}{\beta \cos(\theta)} \tag{4}$$

k is the Sherrer constant (0.89), λ is the X-ray wavelength (nm), β is the peak width at half maximum, and θ is the Bragg diffraction angle. The crystallite sizes of the (111), (220), (311), (400), and (511) for $MnFe_2O_4$ NPs obtained from this equation were found to be about 18, 22, 17, 14, and 29 nm, respectively. The TGA curve of $MnFe_2O_4$ NPs given in Fig. 1c shows no change in the mass during the

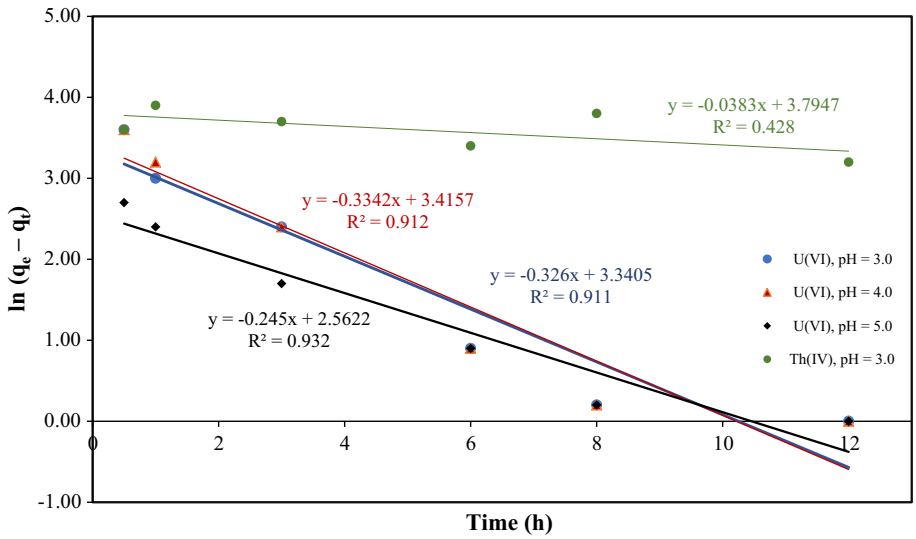

Fig. 5 Pseudo-first order adsorption kinetics of metal ions at 25.0 °C

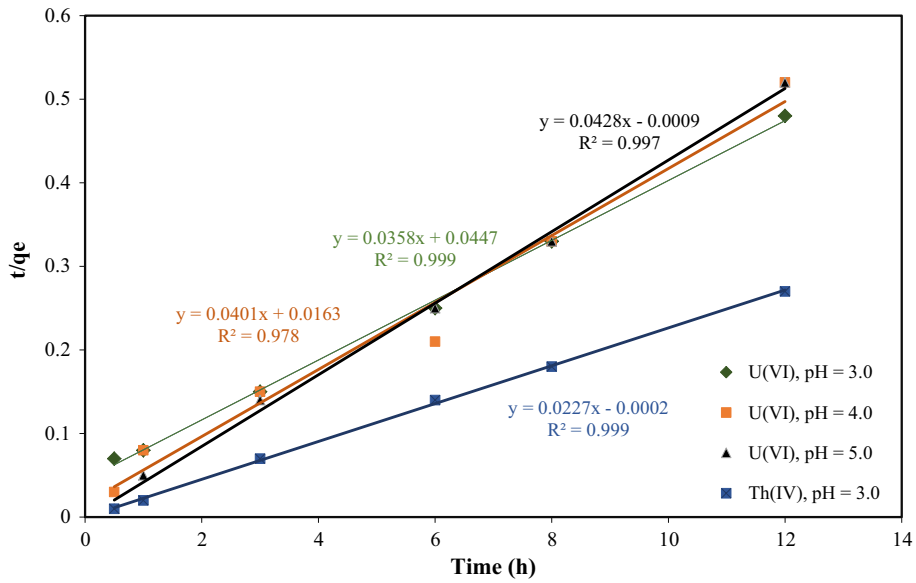

Fig. 6 Pseudo-second order adsorption kinetics of metal ions at 25.0 °C

Table 3 Parameters of pseudo-first order and pseudo second-order kinetic models

Metal ion, pH	Pseudo 1st order			Pseudo 2nd order			q_e (mg g^{-1}) experimental
	q_e (mg g^{-1})	k_1 (h^{-1})	R^2	q_e (mg g^{-1})	k_2 (g mg^{-1} h^{-1})	R^2	
U(VI), pH 3	28.23	0.33	0.91	27.93	0.03	1.00	25.00
U(VI), pH 4	30.44	0.33	0.91	24.94	0.10	0.98	25.09
U(VI), pH 5	12.96	0.26	0.93	23.36	2.04	1.00	24.38
Th(IV), pH 3	44.46	0.04	0.43	44.05	2.58	1.00	43.25

heating process; where the residual mass is 98.32% indicting that $MnFe_2O_4$ NPs are stable over temperature range from 0 to 1000 °C. The DSC thermogram for $MnFe_2O_4$ NPs was recorded under nitrogen (Fig. 1d), shows that the endothermic process corresponds to the phase transition which transforms from orthorhombic to cubic crystal at a temperature range from 10 to 250 °C.

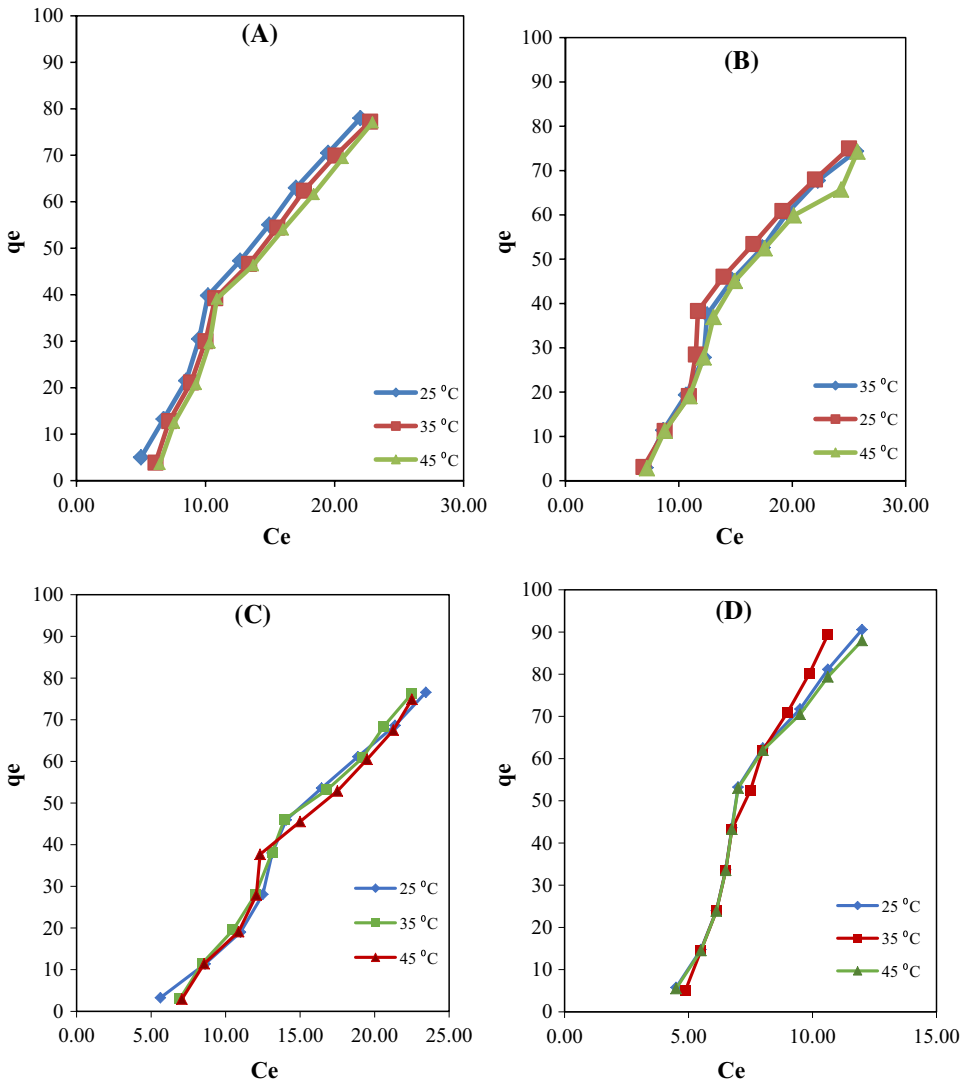

Fig. 7 Adsorption isotherm of **a** U(VI) at pH 3.0, **b** U(VI) at pH 4.0, **c** U(VI) at pH 5.0, and **d** Th(IV) at pH 3.0 by $MnFe_2O_4$ NPs

The morphology of $MnFe_2O_4$ NPs has been investigated by using SEM and TEM; the micrographs of SEM are shown in Fig. 2a. The surfaces of NPs show numerous irregularities in particle size and irregularities plates shape, also TEM images (Fig. 2b) shows miscellaneous plates forms with different size particles, the average dimension distribution of particles processed by "Image-J" program and listed in Table 1, it was proved the sample particles dimensions in the nanoscale. Energy dispersive X-ray spectroscopy (EDXS) gives the type and weight percent of each element presented in the selected point of the sample at SEM micrographs, the percentage of each element after normalization is presented in Table 2. The results show percentage of 1Mn:2O, 1Mn:2Fe, and 2Fe:4O that confirmed with cubic crystal structure of $MnFe_2O_4$, the same results of EDXS analysis for total species of U(VI) or Th(IV) adsorbed on $MnFe_2O_4$ NPs, the C-atom appeared due to hydrolysis species of uranium atom or thorium atom as will be mentioned it in "Effect of solution pH" section.

Zeta-potential is the potential at the plane of shear (located approximately between the compact and diffuse layers) between charged surface and liquid moving with respect to each other [64], and show the surface charge of material. Figure 3 shows that $MnFe_2O_4$ has a negative charge (−7.15 mV), that make it suitable for positive species uptake, such as U(VI) and Th(IV).

Sorption experiments

Effect of sorbent amount

A 5.0 mL of 50.0 ppm of metal ions solution was contacted with various amounts of sorbent (1.0000–5.0000 mg) for 12 h at 25 °C. Figure 4a shows an increase in the % uptake of both ions with increasing in $MnFe_2O_4$ NPs mass due to the increase in the number of adsorbing active sites, so 5.000 mg is a suitable sorbent mass for both ions.

Effect of solution pH

A 5.0 mL of 50.0 ppm of metal ions solution having a pH range of (1.00–7.00) was contacted with 5.0000 mg $MnFe_2O_4$ NPs at 25 °C for 12 h. The results are expressed in Fig. 4b, c, where the maximum uptake of U(VI) with 50% is at pH range (3.0–5.0) and Th(IV) with 90% at pH 3.0. The pH of the solution affects the hydrolysis of U(VI) and Th(IV), at pH > 3.0 UO_2^{2+} produce $UO_2(OH)^+$, $(UO_2)_2(OH)_2^{2+}$, $(UO_2)_3(OH)_5^{3+}$, and $(UO_2)_2(OH)_2$, which decreases sorption efficiency of UO_2^{2+} [65]. Maximum Th^{4+} exists at pH (2.0–3.5), when pH increases the polymeric $Th_m(OH)_n$ is formed, which decreases the sorption at sorbent surface [65, 66]. In addition, pH effect on chemical stability and surface charge of $MnFe_2O_4$ NPs, where positive charge decreases as pH increases until reaching pH 6.0 [67, 68]. Less positive charge on $MnFe_2O_4$ NPs increases the adsorption capacity of positive hydrolyzed metal ions species.

Effect of metal ion concentration

A 5.0 mL of different concentration of U(VI) and Th(IV) solution range (10.0–100.0) ppm at optimized pH conditions 12 h. The results are expressed in Fig. 4d, where the uptake of U(VI) and Th(IV) reaches its maximum at 50.0 ppm. It can be explained by the fact that the rate of accumulation of metal ions on $MnFe_2O_4$ is a function of concentration gradient according to linear driving force law [69]. In addition, the increase in uptake with increase in concentration may be attributed to the improved ratio of total active sites to the metal ions in solution hence these ions interact fully with the active sites.

Effect of contact time

The effect of contact time on metal ions sorption by using $MnFe_2O_4$ NPs was carried out over time intervals (0.5, 1, 3, 6, 8, and 12 h), using 5.0 mL of 50.0 ppm of metal ions solution at optimized pH and 25.0 °C (Fig. 4e) expresses the results. The maximum adsorption capacity (q_m) of metal ions onto $MnFe_2O_4$ NPs increases with increase of contact time, q_m of U(VI) needs 6 h at pH values 3.0 and 4.0, but q_m of U(VI) at pH 5.0 needs 2 h, whereas q_m of Th(IV) needs 1 h.

Kinetics studies

Adsorption kinetics of metal ions consist of two phases: initial phase where adsorption is fast and contributed significantly to equilibrium uptake, and a slower step or the second phase contribute to the metal ions adsorption which is relatively small. There are two kinetic models used to postulate time-dependent adsorption models; pseudo-first-order and pseudo-second-order [70].The pseudo-first-order reaction equation:

$$\ln\left(q_e - q_t\right) = \ln\left(q_e\right) - k_1 t \tag{5}$$

The pseudo-second-order kinetic equation:

$$\frac{t}{q_e} = \frac{1}{k_2 q_e^2} + \frac{1}{q_e} t \tag{6}$$

The results of the pseudo-first-order and pseudo-second-order models are shown in Figs. 5 and 6, respectively. The values of calculated q_e, experimental q_e, and correlation coefficients R^2 are shown in Table 3. The values of R^2, q_e calculated, and q_e experimental fit pseudo-second-order kinetic model more than pseudo-first-order model. The rate-determining step of adsorption metal ions on the surface of sorbents involves physicochemical mechanism, where interactions between two phases of bulk solution and sorbents surface [70, 71]. The value of k_2 (Table 3) shows the uptake of U(VI) by $MnFe_2O_4$ NPs at pH 5.0 (2.04 g mg^{-1} h^{-1}) which reaches to equilibrium faster than uptake of U(VI) at pH 3.0 or 4.0, pH plays a major role in the adsorption of U(VI), the positive charge decreases as pH increases. So, the repulsion force at pH 5.0 is less than the repulsion force at pH 3.0 and pH 4.0. The uptake of Th(IV) by $MnFe_2O_4$ NPs at pH 3.0, (2.58 g mg^{-1} h^{-1}) reaches equilibrium faster than uptake of U(VI) at different pH, because the hydrolysis of Th(IV) and U(VI) as mentioned in "Effect of solution pH" section makes the hydration radius of Th^{4+} less than UO_2^{2+} and other uranyl species that makes adsorption of Th^{4+} easier than UO_2^{2+} [72].

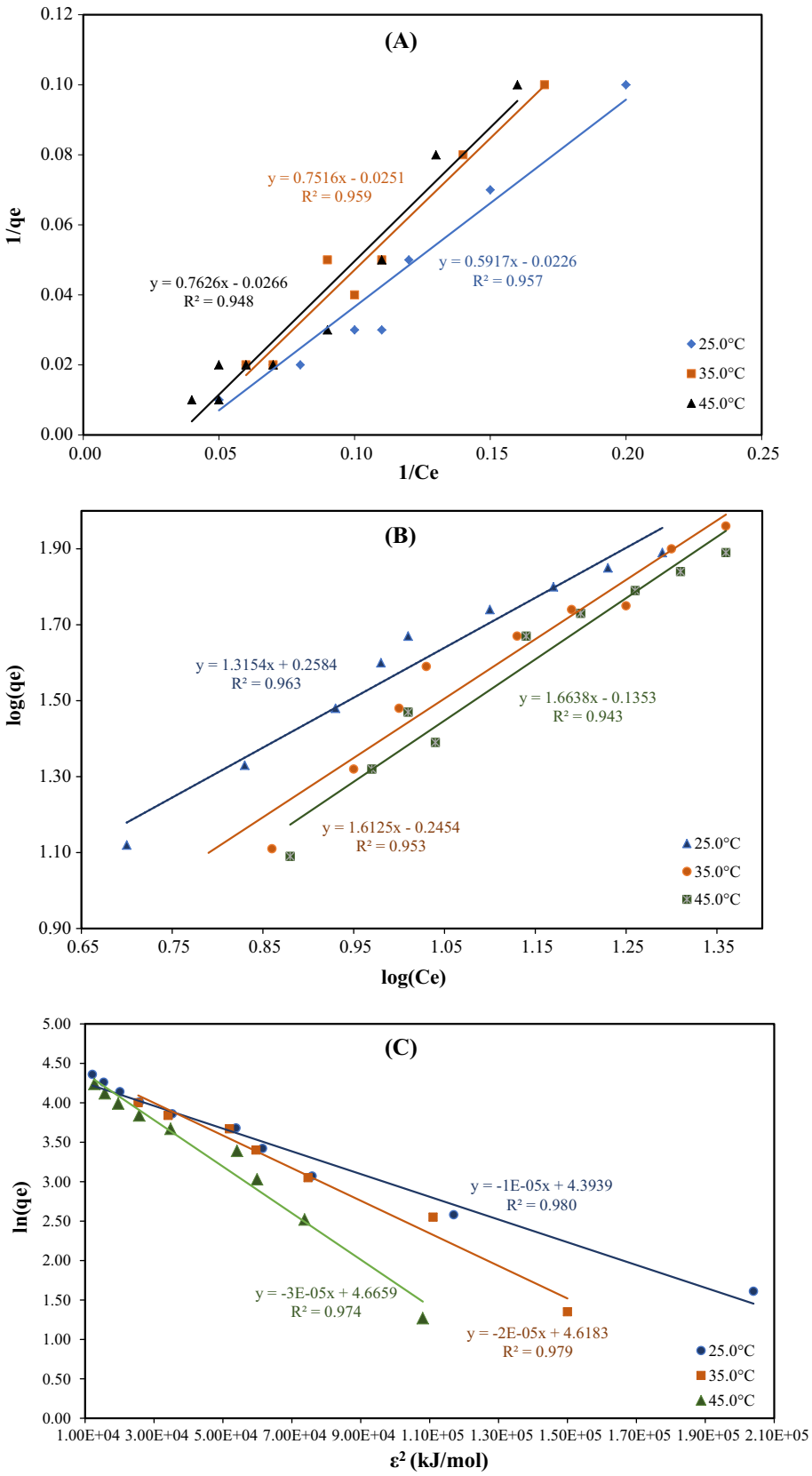

Fig. 8 Plots of linearized adsorption isotherm of U(VI) **a** linearized Langmuir(II), **b** linearized Freundlich, **c** D–R isotherm at pH 3.0 at 25.0 °C, 35.0 °C, and 45.0 °C

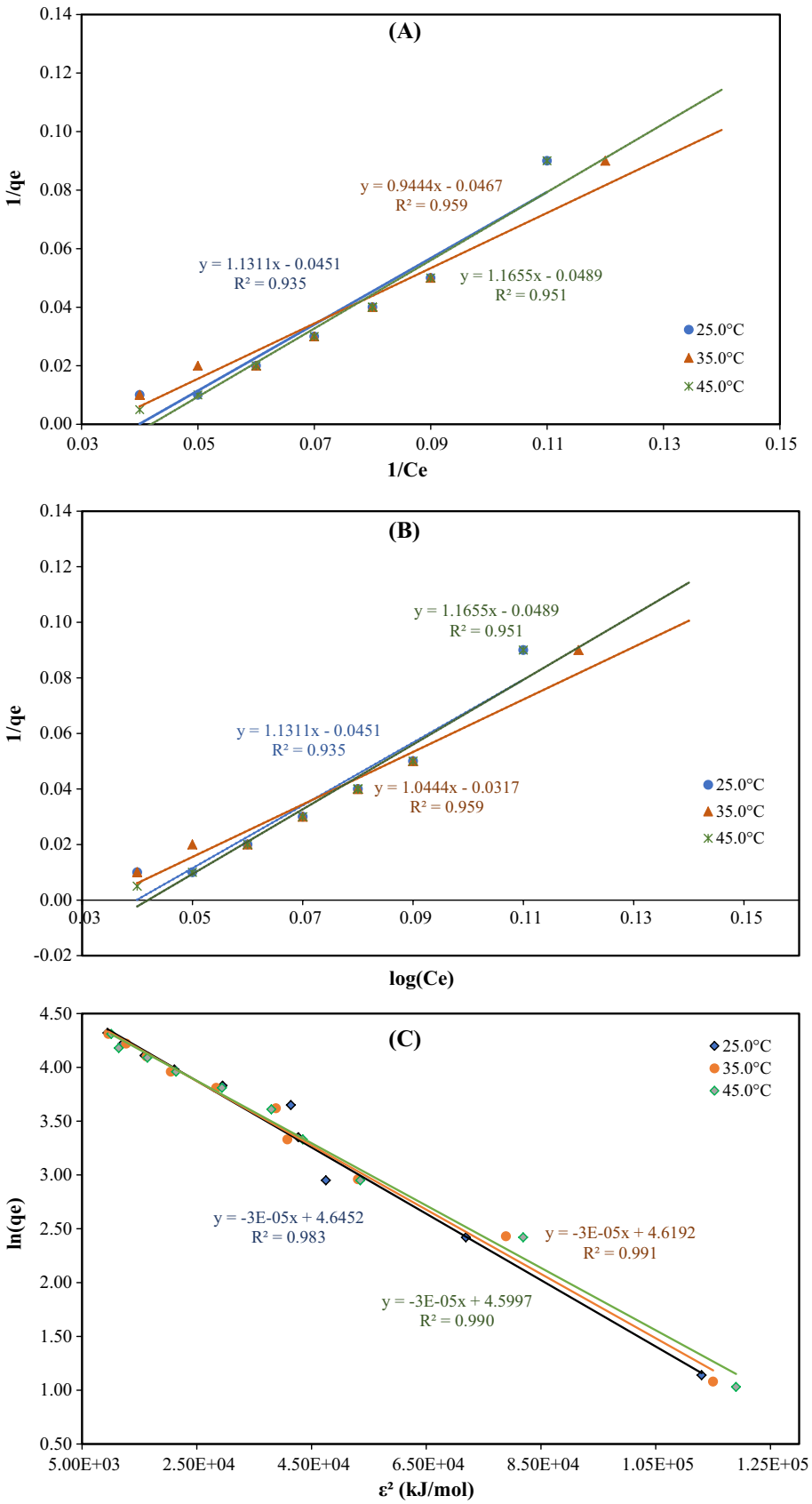

Fig. 9 Plots of linearized adsorption isotherm of U(VI) **a** linearized Langmuir(II), **b** linearized Freundlich, **c** D–R isotherm at pH 4.0 at 25.0 °C, 35.0 °C, and 45.0 °C

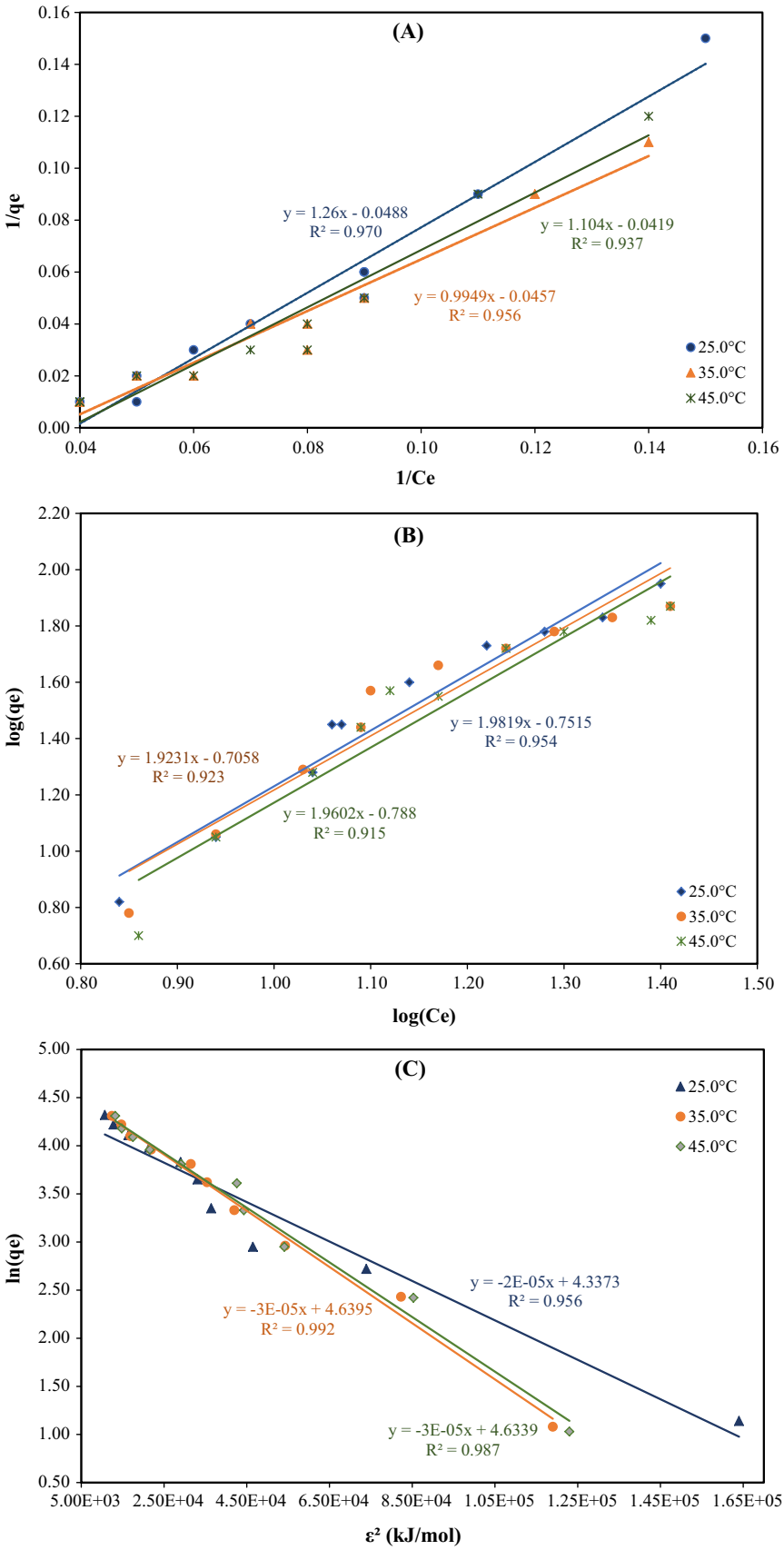

Fig. 10 Plots of linearized adsorption isotherm of U(VI) **a** linearized Langmuir(II), **b** linearized Freundlich, **c** D–R isotherm at pH 5.0 at 25.0 °C, 35.0 °C, and 45.0 °C

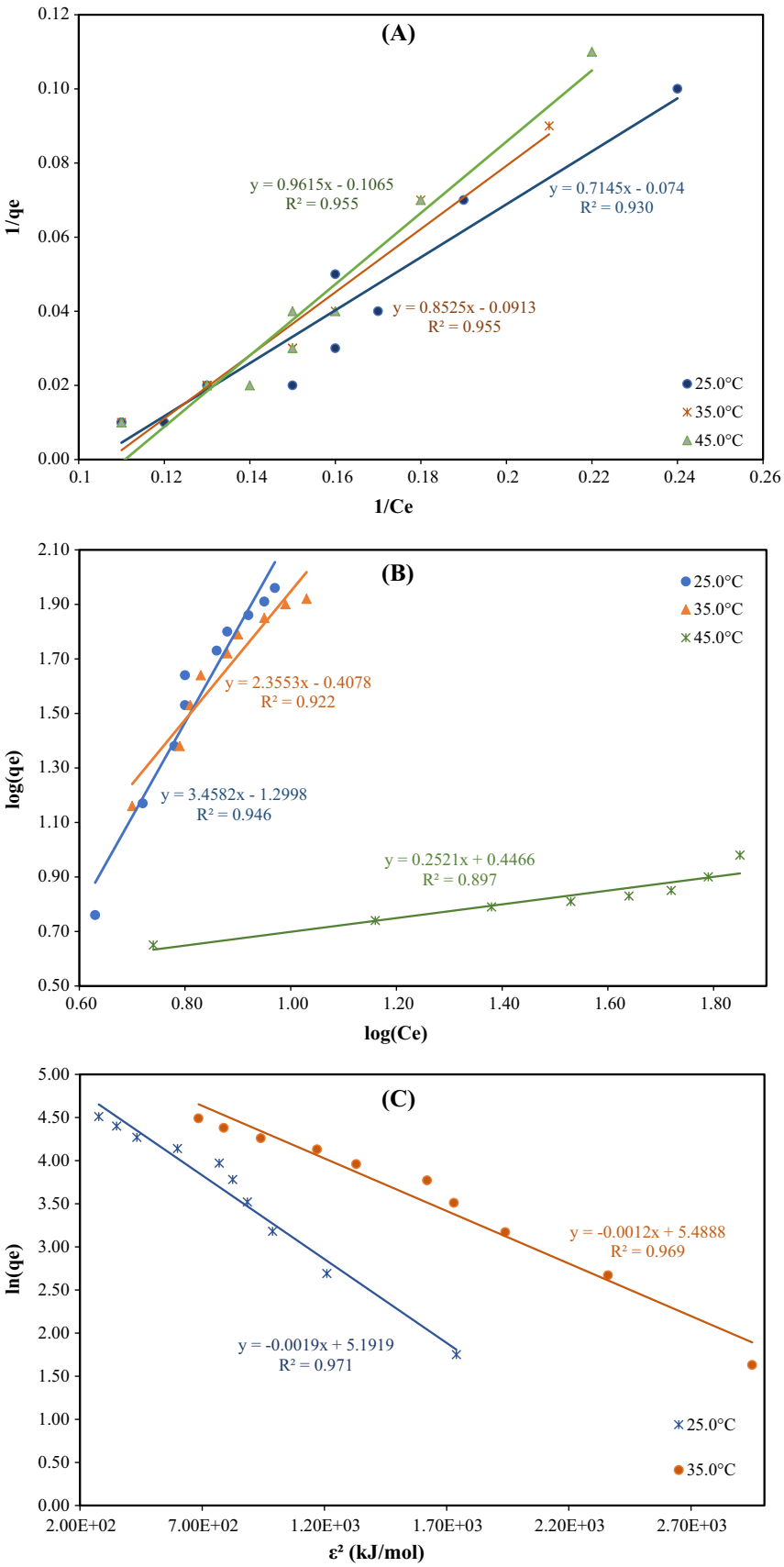

Fig. 11 Plots of linearized adsorption isotherm of Th(IV) **a** Langmuir(II), **b** Freundlich, **c** D–R at pH 3.0 at 25.0 °C and 35.0 °C, **d** D–R isotherm at pH 3.0, 45.0 °C

Fig. 11 (continued)

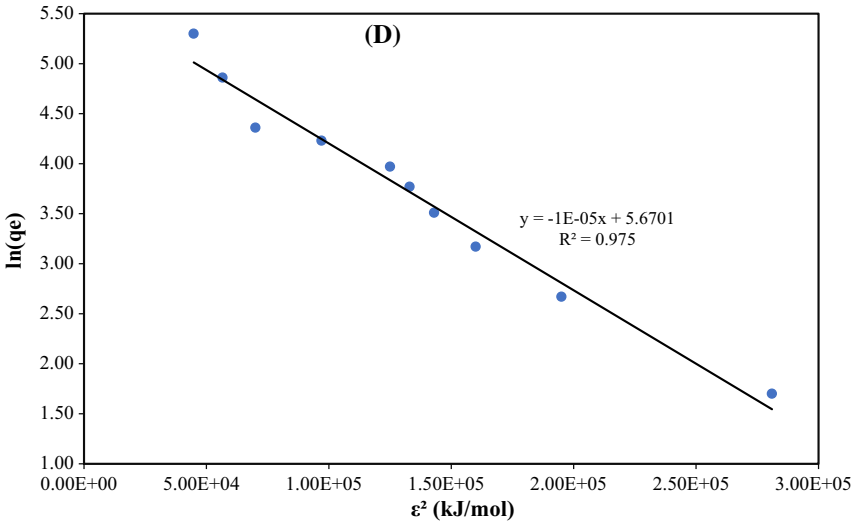

Effect of temperatures

The adsorption isotherm graphs (Fig. 7a–d) explain the sorption process of metal ions by $MnFe_2O_4$ NPs. It undergoes S-type adsorption isotherm, where cooperative adsorption works. The adsorbate interaction at the surface of sorbent is stronger than adsorbate interaction in the bulk, that creates a cluster of multilayers of adsorbate at the surface of sorbent [73].

Adsorption isotherms

The Langmuir, Freundlich and D–R models are commonly used for describing adsorption isotherms. In the present work, the linear Langmuir form (Eq. 7) was used.

$$\frac{1}{q_e} = \left(\frac{1}{q_m K_L}\right)\frac{1}{C_e} + \frac{1}{q_m} \tag{7}$$

The slope and intercept are used to find K_L (L/mg) and q_m (mg/g), and then to find the value of R_L (Eq. 8) that indicates the adsorption nature to be either unfavorable if $R_L > 1$), linear if $R_L = 1$, favorable if $0 < R_L < 1$ and irreversible if $R_L = 0$ [74–76].

$$R_L = \frac{1}{1 + K_L C_o} \tag{8}$$

The linearized Freundlich (Eq. 9) was used to find n (heterogeneity factor) and K_f (the adsorption capacity) value.

$$\log q_e = \log K_f + \frac{1}{n}\log C_e \tag{9}$$

If the (n) value above unity indicates normal sorption, but if the value is less than one, it implies that sorption process is cooperative adsorptions [77, 78].

The linear (D–R) model (Eq. 10) characterizes the physical and chemical features of the adsorption process and it was used to find potential binding energy E (kJ/mol) that describes transferring one mole of adsorbate from solution to sorbent surface [79].

$$\ln(q_e) = \ln(q_m) - \beta\varepsilon^2 \tag{10}$$

$$\varepsilon = RTln\left(1 + \frac{1}{C_e}\right) \tag{11}$$

R is the gas constant (kJ K^{-1} mol^{-1}) and T is the temperature (K), E was calculated by using Eq. (12), where (β) is a constant (mol^2/kJ^2) and (ε) Polanyi potential from Eq. (11).

$$E = \frac{1}{\sqrt{2\beta}} \tag{12}$$

The data of adsorption isotherms from three models for metal ions by $MnFe_2O_4$ NPs are shown in Figs. 8, 9, 10 and

Table 4 Calculated parameters for Langmuir, Freundlich and D–R adsorption isotherm models at different temperatures and pH for U(VI) and Th(IV) ions by $MnFe_2O_4$ NPs

M^{n+}, pH	U(VI), pH 3.0			U(VI), pH 4.0			U(VI), pH 5.0			Th(IV), pH 3.0		
T (°C)	25	35	45	25	35	45	25	35	45	25	35	45
Langmuir												
q_m (mg/g)	44.25	39.84	37.59	22.17	21.41	20.45	20.49	23.87	23.81	13.51	10.95	9.39
K_L (L/mg)	0.05	0.03	0.03	0.04	0.05	0.04	0.04	0.04	0.04	0.10	0.11	0.11
R_L (mg/g)	0.29	0.40	0.40	0.33	0.29	0.33	0.33	0.33	0.33	0.16	0.15	0.15
R^2	0.96	0.96	0.95	0.93	0.96	0.95	0.89	0.91	0.96	0.93	0.96	0.96
Freundlich												
K_f (L/mg)	0.95	0.95	0.94	0.90	0.93	0.90	0.18	0.16	0.20	0.05	0.39	2.80
n	3.87	4.07	7.39	1.13	0.96	0.86	0.50	0.52	0.51	0.29	0.42	3.97
R^2	0.96	0.95	0.94	0.93	0.96	0.95	0.95	0.91	0.92	0.95	0.92	0.90
D–R												
q_m (mg/g)	80.96	101.48	106.26	104.04	101.41	99.45	76.50	103.49	103.91	179.81	241.97	290.09
β (mol^2/kJ^2)	1.00E−05	2.00E−05	3.00E−05	3.00E−05	3.00E−05	3.00E−05	3.00E−05	2.00E−05	3.00E−05	1.90E−03	1.20E−03	1.00E−05
E (kJ/mol)	223.71	158.13	129.10	129.10	129.10	129.10	158.13	129.10	129.10	16.23	20.42	223.71
R^2	0.98	0.98	0.97	0.98	0.99	0.99	0.96	0.99	0.99	0.97	0.97	0.97

Table 5 $\Delta G°$, $\Delta H°$, and $\Delta S°$ for adsorption U(VI) and Th(IV) by $MnFe_2O_4$ NPs at different pH values, 25 °C

Thermodynamic parameters	U(VI)			Th(IV)
	pH 3.0	pH 4.0	pH 5.0	pH 3.0
$\Delta G°$ kJ/mol	1.02	0.67	−0.04	−1.87
$\Delta H°$ kJ/mol	2.86	13.69	−9.54	−2.12
$\Delta S°$ J/K mol	6.18	43.69	−31.88	−0.84

11. The parameters of the Langmuir, Freundlich and D–R models, q_{max}, n, E, and linear regression (R^2) are summarized in Table 4 were used to detect which model explained the adsorption process.

Based on R^2 values of the Langmuir, Freundlich and D–R isotherms models shown in Table 4 and Figs. 8, 9, 10 and 11 are > 0.89 indicating that they describe the adsorption process, but R^2 values of D–R model confirm better representation of experimental data than Langmuir and Freundlich models [80–83]. D–R describes both homogeneous and heterogeneous distribution of adsorbate on sorbents surface by cooperative adsorption [76], also values of (*n*) obtained from Freundlich model (Table 4), suggesting that the adsorption process undergoes a nonlinear sorption process by cooperative adsorption mechanism [77–79, 84]. R_L values obtained from Langmuir model $0 < R_L < 1$, indicate a favorable adsorption of metal ions onto $MnFe_2O_4$ NPs by formation of monolayer at the surface of sorbent [76]. These values give a postulated mechanism about cooperative adsorption, where a monolayer of metal ions formed onto $MnFe_2O_4$ NPs by physical electrostatic adhesion, then the monolayer makes multilayers by chemical bonding with ions in the bulk [84, 85, 86]. Binding energy (*E*) values obtained from D–R model are more 8.00 kJ/mol at different pH and temperatures, indicate that the adsorption mechanism occurred by chemical adsorption process or cooperative adsorption [84, 85, 86].

It is interesting to note that the difference in q_m derived from the Langmuir and q_m derived from D–R models is quite large. The difference may be attributed to the different definition of q_m in the two models. In Langmuir model, q_m represents the maximum adsorption of metal ions at monolayer coverage, whereas in D–R model it represents the maximum adsorption of metal ions at the total specific micropores volume of the sorbent, to form multilayers of sorbent at the surface of sorbent [87, 88]. In this work the value of D–R (q_m) was adopted to describe the adsorption isotherm process, as shown in Table 4 q_m for adsorption U(VI) by $MnFe_2O_4$ NPs at 25 °C, pH 3.0 is 80.96 mg/g and 76.50 mg/g at pH 5.0, but increases to 106.26 mg/g at pH 3.0 and increase to 103.91 at pH 5.0 as temperature increases to 45 °C, indicating an endothermic sorption process and favorable as temperature increases. While q_m of U(VI) at pH

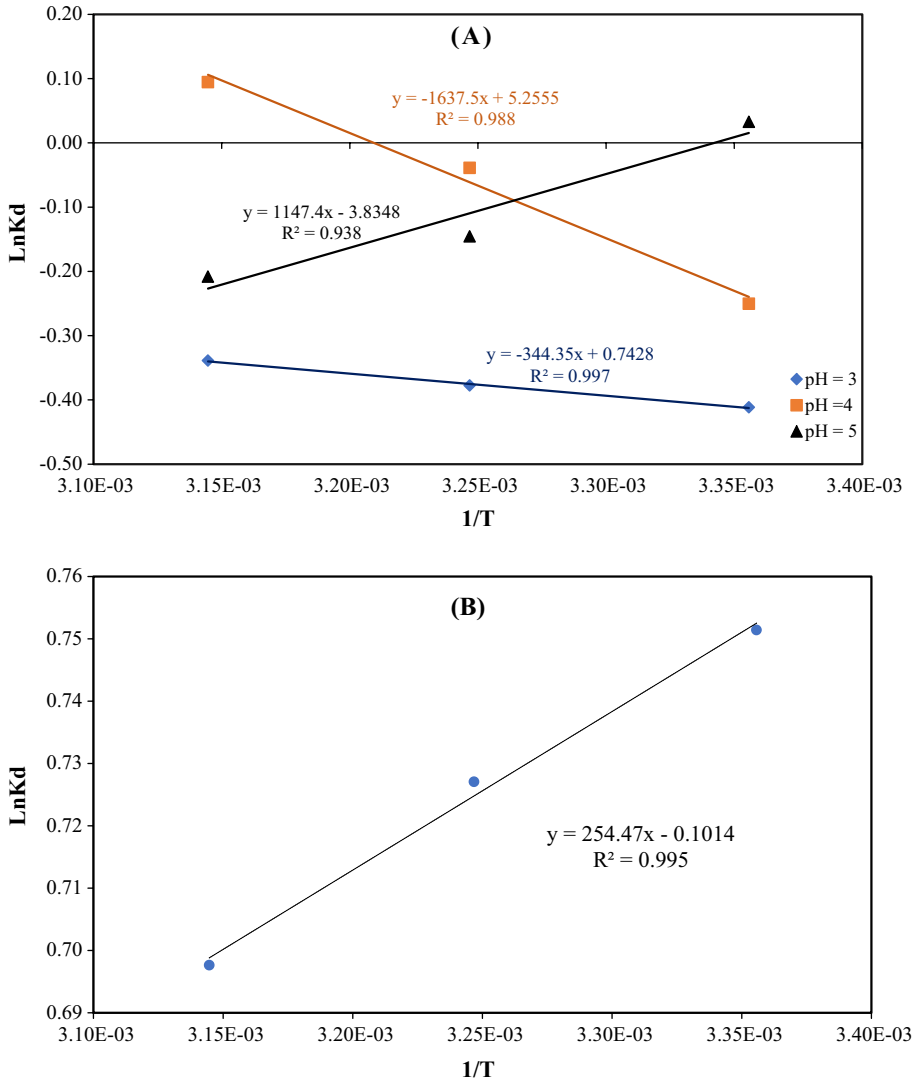

Fig. 12 Plots of Ln K_d Vs. $1/T$ for **a** U(VI) and **b** Th(IV) at pH 3.0

4.0, 25 °C is 104.04 mg/g decreases to 99.45 mg/g as temperature increases to 45 °C, indicates that the sorption process is exothermic process and unfavorable as temperature increases. The q_m for adsorption Th(IV) by $MnFe_2O_4$ NPs at pH 3.0 is 179.81 mg/g at 25 °C, increases to 290.09 mg/g as temperature increases to 45 °C, indicating an endothermic sorption process and favorable as temperature increases. The values of q_m for adsorption Th(IV) > U(VI), suggest that adsorption Th(IV) onto $MnFe_2O_4$ NPs is better than U(VI).

Adsorption thermodynamics

Thermodynamic parameters (Gibbs free energy) $\Delta G°$, (enthalpy) $\Delta H°$, and (entropy) $\Delta S°$ were Calculated at 25 °C and summarized in Table 5. They are obtained by using Van't Hoff Eq. (14) where K_d calculated by using equation. The slope of lnKd Vs. 1/T, (Fig. 12a and b) is $-\Delta H°/R$ and intercept is $\Delta S°/R$ then $\Delta G°$ obtained by using Eq. (15) as shown

$$K_d = \frac{q_e}{C_e} \tag{13}$$

$$\mathrm{Ln}K_d = \frac{\Delta S°}{R} - \frac{\Delta H°}{RT} \tag{14}$$

$$\Delta G° = \Delta H° - T\Delta S° \tag{15}$$

Table 6 Maximum adsorption capacity q_m (mg/g) of U(VI)/Th(IV) metal ions on various nanosorbents with present work $MnFe_2O_4$ NPs at 25 °C

Metal ions	Nanosorbent	q_m	pH	References
Th(IV)	Titanate nanotubes	233.00	3.0	[88]
Th(IV)	Magnetic multi-walled carbon nanotubes	33.35	3.0	[80]
U(VI)	Ion-imprinted chitosan/PVA nanoparticles	0.66	5.0	[81]
U(VI)	Phosphonate grafted mesoporous carbon	150.00	4.0	[82]
U(VI)	Silica-coated magnetic Fe_3O_4 nanoparticles	12.33	1.0	[83]
Th(IV)	Fe_3O_4 magnetic ion-imprinted chitosan	147.10	4.0	[89]
U(VI)	Fe_3O_4 magnetic carboxymethyl chitosan nano-particles functionalized with ethylenediamine	175.40	4.5	[90]
U(VI)	Graphene oxide–manganese dioxide nanoparticles α-MnO_2/GO	185.20	4.0	[91]
U(VI)	Graphene oxide–manganese dioxide nanoparticles γ-MnO_2/GO	66.80	4.0	[91]
Th(IV)	Graphene oxide–manganese dioxide nanoparticles α-MnO_2/GO	497.50	4.0	[91]
Th(IV)	Graphene oxide–manganese dioxide nanoparticles γ-MnO_2/GO	408.80	4.0	[91]
Th(IV)	Amino-Fe_3O_4 magnetic glycidyl methacrylate nanoparticles	50.89	3.7	[92]
Th(IV)	Amino-Fe_3O_4 magnetic glycidyl divinylbenzene nanoparticles	68.98	3.7	[92]
Th(IV)	Polyacrylonitrile composite nanofiber adsorbent	249.4 (45 °C)	6.0	[92]
Th(IV)	Magnetic Fe_3O_4/SiO_2/PVA/aminopropyltriethoxysilane (APTES) nanoparticles	62.50	5.0	[93]
U(VI)	Amberlite IR120 by magnetic nano iron-oxide	10.36	3.5	[94]
U(VI)	$MnFe_2O_4$	80.96	3	Present work
		104.04	4	
		76.50	5	
Th(IV)	$MnFe_2O_4$	179.81	3.0	Present work

According to Van't Hoff plot, the adsorption processes of U(VI) on $MnFe_2O_4$ NPs at pH 3.0 and 4.0 are classified as endothermic physical process, but the adsorption of U(VI) on $MnFe_2O_4$ at pH 5.0 and Th(IV) on $MnFe_2O_4$ NPs at pH 3.0 are classified as exothermic physical process.

As shown in Table 5 $\Delta H°$ of Th(IV) at pH 3.0 and U(VI) at pH 5.0 is negative, indicates that the adsorption process is exothermic process, and negative $\Delta S°$ indicates a stable arrangement of metal ions on $MnFe_2O_4$ NPs surfaces, and the adsorbed metal ions on $MnFe_2O_4$ NPs surfaces are more ordered than metal ions in the bulk solution, while negative $\Delta G°$ means that the adsorption process is favorable process. Positive $\Delta H°$ of the adsorption of U(VI) at pH 3.0 and 4.0 on the $MnFe_2O_4$ NPs indicates an endothermic process, and positive $\Delta S°$ indicates less stable arrangement of U(VI) ions onto $MnFe_2O_4$ NPs surfaces and the adsorbed U(VI) on $MnFe_2O_4$ surface is less ordered than U(VI) in the bulk solution, while positive $\Delta G°$ means the adsorption process is less favorable process [74–76]. This behavior explains due to the hydrolyzed species of both U(VI) and Th(IV) at these pH values, and the interaction of hydrolyzed species with surface charge of $MnFe_2O_4$ NPs at the same pH.

Comparative study

Based on optimization conditions results, kinetic data, and thermodynamic results, $MnFe_2O_4$ NPs have special conditions work and have unique results describe adsorption of U(VI) and Th(IV). Table 6 shows a suitable efficiency of U(VI) and Th(IV) removal by $MnFe_2O_4$ NPs comparison with other nanosorbent at different pH and 25 °C.

Reusability and stability of $MnFe_2O_4$ NPs

The reusability of $MnFe_2O_4$ NPs was investigated by desorption test by using batch methods started by loading of metal ions onto $MnFe_2O_4$ NPs surfaces, then the metal ions leached using 5 cycles with different intervals of time (Fig. 13a and b) shows the desorption capacity of U(VI) and Th(IV) from $MnFe_2O_4$ NPs using 0.10 M HCl, HNO_3, NaCl, Na_2CO_3, and

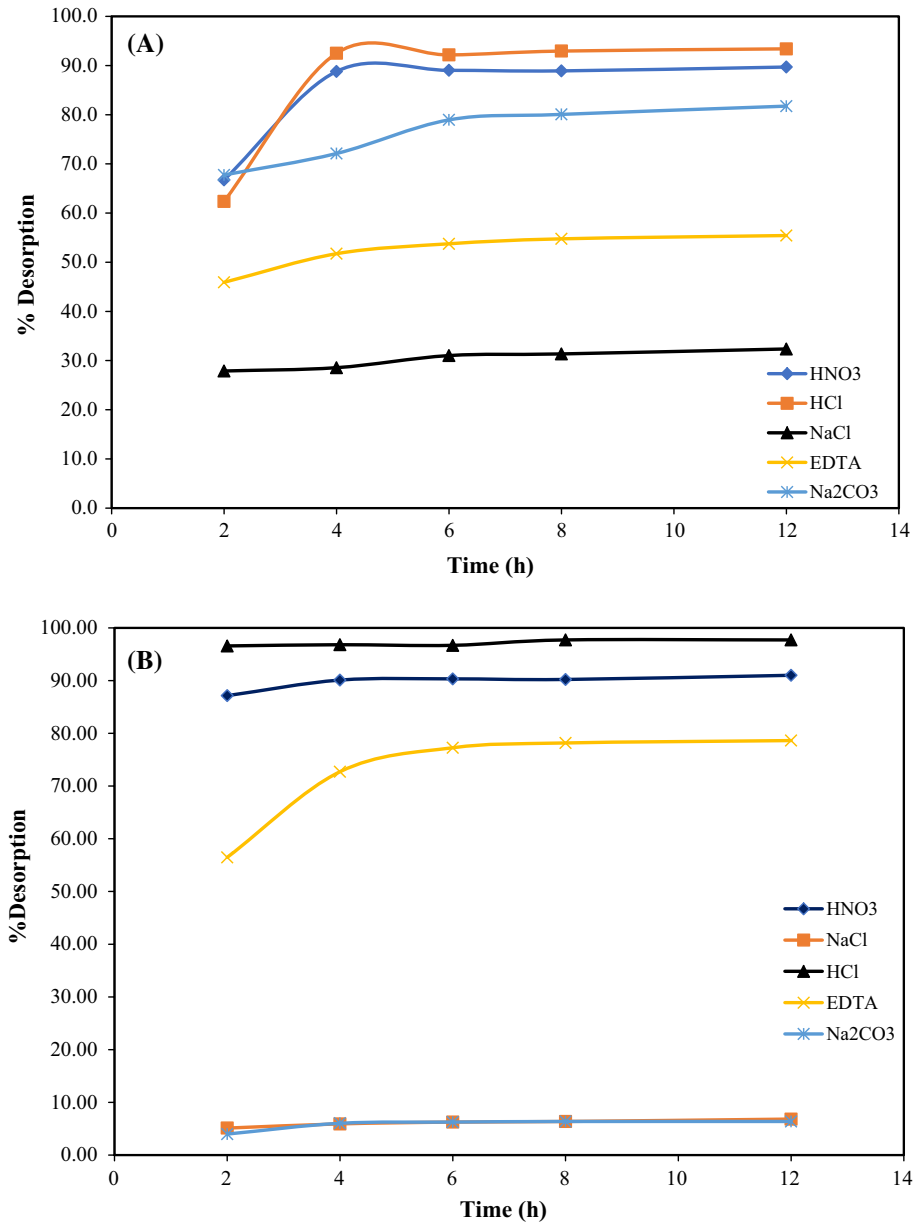

Fig. 13 Desorption of **a** U(VI) and **b** Th(IV) loaded on $MnFe_2O_4$ NPs

EDTA eluents. They have different pH values effect on desorption process and stability of sorbents. The results show that the highest desorption of U(VI) was 92.50% by using HCl eluent during 4 h (Fig. 13a), and the highest desorption of Th(IV) was 96.80% by using HCl eluent during 2 h (Fig. 13b).

Conclusion

$MnFe_2O_4$ nanoparticles were fabricated in nanoscale using co-precipitation methods in a green and easy way. It were used as a sorbent to remove of U(VI) and Th(IV) from water, the adsorption contact time was fast to moderate range (1–6 h). The pH of the solutions plays a major role in determining the maximum adsorption capacity metal ions, pH 3.0 was the best condition to remediate Th(IV) and pH 3.0–5.0 to remediate U(VI). The equilibrium kinetics of U(VI) and Th(IV) adsorption were explained using the pseudo-second-order equilibrium model. The adsorption thermodynamics of removal U(VI) at pH 3.0 and 4.0 by $MnFe_2O_4$ NPs is

endothermic process while the adsorption thermodynamics of U(VI) at pH 5.0 and Th(IV) at pH 3.0 by $MnFe_2O_4$ NPs is an exothermic process. $MnFe_2O_4$ NPs are suitable sorbents with a high reusability feature for U(VI) and Th(IV) using different eluents with different pH values.

Acknowledgements We would like to thank the School of Graduate Studies at The University of Jordan, and The German Academic Exchange Service for financial support.

References

1. Bamdad H, Hawboldt K, MacQuarrie S (2018) A review on common adsorbents for acid gases removal: focus on biochar. Renew Sustain Energy Rev 81:1705–1720
2. Yua C, Han X (2015) Adsorbent material used in water treatment—a review. 2nd international workshop on materials engineering and computer sciences (IWMECS 2015)
3. Singh NB, Nagpal G, Agrawal S (2018) Water purification by using adsorbents: a review. Environ Technol Innov 11:187–240
4. Burakov AE, Galunin EV, Burakova IV, Kucherova AE, Agarwal S, Tkachev AG, Gupta VK (2018) Ecotoxicology and environmental safety adsorption of heavy metals on conventional and nanostructured materials for wastewater treatment purposes: a review. Ecotoxicol Environ Saf 148:702–712
5. Zhang L, Zeng Y, Cheng Z (2016) Removal of heavy metal ions using chitosan and modified chitosan: a review. J Mol Liq 214:175–191
6. Vakili M, Rafatullah M, Salamatinia B, Zuhairi A, Hakimi M, Bing K, Gholami Z, Amouzgar P (2014) Application of chitosan and its derivatives as adsorbents for dye removal from water and wastewater: a review. Carbohydr Polym 113:115–130
7. Yim MS, Ismail AF (2015) Investigation of activated carbon adsorbent electrode for electrosorption-based uranium extraction from seawater. Nucl Eng Technol 47:579–587
8. Khalili FI, Salameh NH, Shaybe MM (2013) Sorption of uranium(VI) and thorium(IV) by Jordanian bentonite. J Chem 586136:1–13
9. Khalili F, Al-Shaybe M (2010) Adsorption of thorium(IV) and uranium(VI) by Tulul al-Shabba zeolitic tuff, Jordan. Jordan J Earth Environ Sci 2(1):108–119
10. Rushdi IY, El-Eswed B, Alshaaer M, Khalili F, Khouri H (2009) The influence of using Jordanian natural zeolite on the adsorption, physical, and mechanical properties of geopolymers products. J Hazard Mater 165:379–387
11. Zhang Y, Li Y, Ning Y, Liu D, Tang P, Yang Z, Lu Y, Wang X (2018) Adsorption and desorption of uranium(VI) onto humic acids derived from uranium-enriched lignites. Water Sci Technol 77(4):920–930
12. Chassary P, Vincent T, Guibal E (2004) Metal anion sorption on chitosan and derivative materials: a strategy polymer modification and optimum use. React Funct Polym 60:137–149
13. Kalin M, Wheeler WN, Meinrath G (2005) The removal of uranium from mining waste water using algal/microbial biomass. J Environ Radioact 78:151–177
14. Benes P, Kratzer K, Vlckova S, Sebestova E (1998) Adsorption of uranium on clay and the effect of humic substances. Radiochim Acta 82:367–373
15. Bhatnagar A, Vilar VJ, Botelho CM, Boaventura RM (2011) A review of the use of red mud as adsorbent for the removal of toxic pollutants from water and wastewater. Environ Technol 32:231–249
16. Gomes AF, Lopez S, Dina L, Ladeira A, Claudia Q (2012) Characterization and assessment of chemical modifications of metal-bearing sludge's arising from unsuitable disposal. J Hazard Mater 200:418–425
17. Mahmoud MA (2013) Removal of uranium(VI) from aqueous solution using low cost and eco-friendly adsorbents. J Chem Eng Process Technol 4(6):2157–2160
18. Huang G, Peng W, Yang S (2018) Synthesis of magnetic chitosan/graphene oxide nanocomposites and its application for U(VI) adsorption from aqueous solution. J Radioanal Nucl Chem 317(1):337–344
19. Zhao X, Tang Z, Zhao T, Wang H, Wang P, Wu F, Giesy JP (2016) Magnetic nanoparticles interaction with humic acid: in the presence of surfactants. Environ Sci Technol 50(16):8640–8648
20. Das D, Sureshkumar M, Koley S, Mithal N, Pillai C (2010) Sorption of uranium on magnetite nanoparticles. J Radioanal Nucl Chem 285:447–454
21. Lindner H, Schneider E (2015) Review of cost estimates for uranium recovery from seawater. Energy Econ 49:9–22
22. Imran A (2012) New generation adsorbents for water treatment. Chem Rev 112(10):5073–5091
23. Khajeh M, Laurent S, Dastafkan K (2013) Nanoadsorbents: classification, preparation, and applications (with emphasis on aqueous media). Chem Rev 113(10):7728–7768
24. Upadhyayula VKK, Deng S, Mitchell MC, Smith GB (2009) Application of carbon nanotube technology for removal of contaminants in drinking water: a review. Sci Total Environ 408(1):1–13
25. Nasreen SAAN, Sundarrajan S, Nizar SAA, Ramakrishna S (2019) Nanomaterials: solutions to water-concomitant challenges. Membranes 9(3):1–21
26. Li X, Elliott DW, Zhang W, Li X, Elliott DW, Zhang W (2006) Zero-valent iron nanoparticles for abatement of environmental pollutants: materials and engineering aspects zero-valent iron nanoparticles for abatement of environmental pollutants: materials and engineering aspects. Crit Rev Solid State 31(4):111–122
27. Liu D, Liu Z, Wang C, Lai Y (2016) Removal of uranium(VI) from aqueous solution using nanoscale zero-valent iron supported on activated charcoal. J Radioanal Nucl Chem 310(3):1131–1137
28. Addleman SR, Chouyyok W, Warner CL, Mackie KM, Warner MG, Gill G (2016) Nanostructured metal oxide sorbents for the collection and recovery of uranium from seawater. Ind Eng Chem Res 55(15):4195–4207
29. Nekhunguni PM, Tavengwa NT, Tutu H (2017) Sorption of uranium(VI) onto hydrous ferric oxide-modified zeolite: assessment of the effect of pH, contact time, temperature, selected cations and anions on sorbent interactions. J Environ Manag 204:571–582. https://doi.org/10.1016/j.jenvman.2017.09.034
30. Zhu M, Wang Y, Meng D, Qin X, Diao G (2012) Hydrothermal synthesis of hematite nanoparticles and their electrochemical properties. J Phys Chem C 116:16276–16285
31. Dave PN, Chopda LV (2014) Application of iron oxide nanomaterials for the removal of heavy metals. J Nanotechnol 398569:1–14
32. Naseri MG, Saion BE, Kamali A (2012) An overview on nanocrystalline $ZnFe_2O_4$, $MnFe_2O_4$, and $CoFe_2O_4$ synthesized by a thermal treatment method. ISRN Nanotechnol 2012:1–11
33. Dinesha BL, Sharanagouda H, Udaykumar N, Ramachandr CT, Dandekar AB (2017) Removal of pollutants from water/waste water using nano-adsorbents: a potential pollution mitigation. Int J Curr Microbiol Appl Sci 6(10):4868–4872
34. Li B, Chen L (2012) Application of magnetic molecularly imprinted polymers in analytical chemistry. Anal Methods 4(9):2613–2621

35. Schuth F, Lu A, Salabas EL (2007) Magnetic nanoparticles: synthesis, protection, functionalization, and application. Angew Chem Int Ed 46:1222–1244
36. Harizanova R, Avramova I, Wisniewski W, Avdeev G, Tzankov D, Georgieva M, Gugov I, Russel C (2018) EBSD-investigation and magnetic properties of manganese ferrite crystallized in a sodium-silicate glass. CrystEngComm 20:4268–4276
37. Soliman S, Elfalaky A (2013) Theoretical investigation of $MnFe_2O_4$. J Alloys Compd 580:401–406
38. Deraz NM, Alarifi A (2012) Novel preparation and properties of magnesioferrite nanoparticles. J Anal Appl Pyrol 97:55–61
39. Gajbhiye NS, Balaji G, Ghafari M (2002) Magnetic properties of $MnFe_2O_4$ nanoparticles. Phys Stat Sol (a) 189(2):357–361
40. Jacintha AM, Umapathy V, Neeraja P, Rajkumar SR (2017) Synthesis and comparative studies of $MnFe_2O_4$ nanoparticles with different natural polymers by sol–gel method: structural, morphological, optical, magnetic, catalytic and biological activities. J Nanostruct Chem 7:375–387
41. Vignesh RH, Sankar KV, Amaresh S, Lee YS, Selvan RK (2015) Synthesis and characterization of $MnFe_2O_4$ nanoparticles for impedometric ammonia gas sensor. Sens Actuators B 220:50–58
42. Hu J, Chen G (2005) Fast removal and recovery of Cr(VI) using surface-modified jacobsite ($MnFe_2O_4$) nanoparticles. Langmuir 21(24):11173–11179
43. Wu R, Qu J (2005) Removal of water-soluble azo dye by the magnetic material $MnFe_2O_4$. J Chem Technol Biotechnol 27:20–27
44. Naseri MG, Saion EB, Ahanger HA, Hashim M, Shaari AH (2011) Synthesis and characterization of manganese ferrite nanoparticles by thermal treatment method. J Magn Magn Mater 32:1745–1749
45. Gharagozlou M (2009) Synthesis, characterization and influence of calcination temperature on magnetic properties of nanocrystalline spinel Co-ferrite prepared by polymeric precursor method. J Alloys Compd 486(1):660–665
46. Chen D, Zhang Y, Kang Z (2013) A low temperature synthesis of $MnFe_2O_4$ nanocrystals by microwave-assisted ball-milling. Chem Eng J 215–216:235–239
47. Lu A, Hui E, Salabas L, Schüth F (2007) Magnetic nanoparticles: synthesis, protection, functionalization, and application. Angew Chem Int Ed 46(8):1222–1244
48. Dhakal T, Mukherjee D, Hyde R, Mukherjee P, Phan MH, Srikanth H, Witanachchi S (2010) Magnetic anisotropy and field switching in cobalt ferrite thin films deposited by pulsed laser ablation. J Appl Phys 107(5): Article ID 053914-(1–6)
49. Mornet S, Vasseur S, Grasset F, Verveka P, Goglio G, Demourgues A, Portier J, Pollert E, Duguet E (2006) Magnetic nanoparticle design for medical applications. Prog Solid State Chem 34(2–4):237–247
50. Gupta KA, Gupta M (2005) Synthesis and surface engineering of iron oxide nanoparticles for biomedical applications. Biomaterials 26(18):3995–4021
51. Vignesh RH, Sankara KV, Amareshb S (2015) Synthesis and characterization of $MnFe_2O_4$ nanoparticles for impedometric ammonia gas sensor. Sens Actuators B Chem 220:1–18
52. Rathorea D, Mitra S (2016) $MnFe_2O_4$ as a gas sensor towards SO_2 and NO_2 gases. AIP Conf Proc 1728:020166-1–020166-4
53. Pal M, Rakshit R, Mandal K (2014) Surface modification of $MnFe_2O_4$ nanoparticles to impart intrinsic multiple fluorescence and novel photocatalytic properties. ACS Appl Mater Interfaces 6:4903–4910
54. Lu HA, Schmidt W, Matoussevitch N, Bonnermann H, Spliethoff B, Tesche B, Bill E, Kiefer W, Schuth F (2004) Nanoengineering of a magnetically separable hydrogenation catalyst. Angew Chem 116:4403–4409
55. Lu F, Astruc D (2018) Nanomaterials for removal of toxic elements from water. Coord Chem Rev 356:147–164
56. Dubey S, Banerjee S, Upadhyay SN, Sharma YC (2017) Application of common nano-materials for removal of selected metallic species from water and wastewaters: a critical review. J Mol Liq 240:656–677
57. Qu X, Alvarez PJJ, Li Q (2013) Applications of nanotechnology in water and wastewater treatment. Water Res 47(12):3931–3946
58. Khan H, Haleem M, Warwick P, Evans N (2006) Spectrophotometric determination of uranium with arsenazo-III in perchloric acid. Chemosphere 63(7):1165–1169
59. Savvin SB (1961) Analytical use of arsenazo(III), determination of thorium, zirconium, uranium and rare earth elements, vol 8. Pergmon Press Ltd, Oxford, pp 673–685
60. Cali E, Qi J, Preedy O, Chen S, Boldrin D, Branford WR, Vandeperre L, Ryan MP (2018) Functionalised magnetic nanoparticles for uranium adsorption with ultra-high capacity and selectivity. J Mater Chem A 6:3063–3073
61. Jing Z, Wu S (2004) Synthesis and characterization of monodisperse hematite nanoparticles modified by surfactants via hydrothermal approach. Mater Lett 58:3637–3640
62. Waldron RD (1955) Infrared spectra of ferrites. Phys Rev 99:1727–1735
63. Torapava N, Persson I, Eriksson L, Lundberg D (2009) Hydration and hydrolysis of thorium(IV) in aqueous solution and the structures of two crystalline thorium(IV) hydrates. Inorg Chem 48(24):11712–11723
64. Szymczyk A, Fievet P, Mullet M, Reggiani JC, Pagetti J (1998) Comparison of two electrokinetic methods—electroosmosis and streaming potential—to determine the zeta-potential of plane ceramic membranes. J Membr Sci 143:189–195
65. Nethaji S, Sivasamy A, Mandal AB (2013) Adsorption isotherms, kinetics and mechanism for the adsorption of cationic and anionic dyes onto carbonaceous particles prepared from *Juglans regia* shell biomass. Int J Environ Sci Technol 10:231–242
66. Szabo Z, Toraishi T, Vallet V, Grenthe I (2006) Solution coordination chemistry of actinides: thermodynamics, structure and reaction mechanisms. Coord Chem Rev 250:784–815
67. Zhang L, Chen Q, Zheng J, Yang Q, Dang Z (2019) Insights into the glyphosate adsorption behavior and mechanism by a $MnFe_2O_4$@cellulose-activated carbon magnetic hybrid. ACS Appl Mater Interfaces 11(17):15478–15488
68. Xiao Y, Liang H, Wang Z (2013) $MnFe_2O_4$/chitosan nanocomposites as a recyclable adsorbent for the removal of hexavalent chromium. Mater Res Bull 48(10):3910–3915
69. Bhaumik M, Setshedi K, Maity A, Onyango MS (2013) Chromium(VI) removal from water using fixed bed column of polypyrrole/Fe_3O_4 nanocomposite. Sep Purif Technol 110:11–19
70. Robati D (2013) Pseudo-second-order kinetic equations for modeling adsorption systems for removal of lead ions using multi-walled carbon nanotube. J Nanostructure Chem 3(1):55–61
71. Giles CH, Smith D, Huitson A (1974) A general treatment and classification of the solute adsorption isotherm. I. Theoretical. J Colloid Interface Sci 47(3):755–765
72. Humelnicu D, Dinu MV, Dragan ES (2011) Adsorption characteristics of UO_2^{2+} and Th^{4+} ions from simulated radioactive solutions onto chitosan/clinoptilolite sorbents. J Hazard Mater 185(1):447–455
73. Khalili FI, Al-Kakah MS, Ayoub MM, Ismail LS (2019) Sorption of Pb(II), Cd(II) and Zn(II) ions from aqueous solution using Jordanian kaolinite modified by the amino acids methionine or cysteine. Desalin Water Treat 151:280–294
74. Salameh SIY, Khalili FI, Al-Dujaili AH (2017) Removal of U(VI) and Th(IV) from aqueous solutions by organically modified diatomaceous earth: evaluation of equilibrium, kinetic and thermodynamic data. Int J Miner Process 168:9–18

75. Dada AO, Olalekan AP, Olatunya AM, Dada O (2012) Langmuir, Freundlich, Temkin and Dubinin–Radushkevich isotherms studies of equilibrium sorption of Zn^{2+} unto phosphoric acid modified rice husk. IOSR J Appl Chem 3(1):38–45
76. Liu S (2015) Cooperative adsorption on solid surfaces. J Colloid Interface Sci 450(2015):224–238
77. Bowman BT (1981) Anomalies in the log Freundlich equation resulting in deviations in adsorption *k* values of pesticides and other organic compounds when the system of units is changed. J Environ Sci Health B 16(2):113–123
78. Ayawei N, Ebelegi AN, Wankasi D (2017) Modelling and interpretation of adsorption isotherm. J Chem 3039817:1–11
79. Tretiakov KV, Bishop KJM, Kowalczyk B, Jaiswal A, Poggi MA, Grzybowski BA (2009) Mechanism of the cooperative adsorption of oppositely charged nanoparticles. J Phys Chem A 113(16):3799–3803
80. Liu P, Qi W, Du Y, Li Z, Wang J, Bi J, Wu W (2014) Adsorption of thorium(IV) on magnetic multi-walled carbon nanotubes. Sci China Chem 57(11):1483–1490
81. Mirzabe GH, Keshtkar AR (2015) Application of response surface methodology for thorium adsorption on PVA/Fe_3O_4/SiO_2/APTES nanohybrid adsorbent. J Ind Eng Chem 26(25):277–285
82. Husnain SM, Kim HJ, Um W, Chang YY, Chang YS (2017) Superparamagnetic adsorbent based on phosphonate grafted mesoporous carbon for uranium removal. Ind Eng Chem Res 56(35):9821–9830
83. Sadeghi S, Azhdari H, Arabi H, Moghaddam AZ (2012) Surface modified magnetic Fe_3O_4 nanoparticles as a selective sorbent for solid phase extraction of uranyl ions from water samples. J Hazard Mater 215–216:208–216
84. Skopp J (2009) Derivation of the Freundlich adsorption isotherm from kinetics. J Chem Educ 86(11):1341–1344
85. Li G, Xu H, Li J, Chen C, Ren X (2016) Interaction of Th(IV) with graphene oxides: batch experiments, XPS investigation, and modeling. J Mol Liq 213:58–68
86. Reed DA, Keitz BK, Oktawiec J, Mason JA, Runcevski T, Xiao DJ, Long JR (2017) A spin transition mechanism for cooperative adsorption in metal–organic frameworks. Nature 550:96–100
87. Binabaj MA, Nowee SM, Ramezanian N (2018) Comparative study on adsorption of chromium(VI) from industrial wastewater onto nature-derived adsorbents (brown coal and zeolite). Int J Environ Sci Technol 15(7):1509–1520
88. Liu J, Luo M, Yuan Z, Ping A (2013) Synthesis, characterization, and application of titanate nanotubes for Th(IV) adsorption. J Radioanal Nucl Chem 298(2):1427–1434
89. Huang G, Chen Z, Wang L, Lv T, Shi J (2016) Removal of thorium(IV) from aqueous solution using magnetic ion-imprinted chitosan resin. J Radioanal Nucl Chem 310(3):1265–1272
90. Zhou L, Zou H, Wang Y, Huang Z, Wang Y, Luo T, Liu Z, Adesina AA (2016) Adsorption of uranium(VI) from aqueous solution using magnetic carboxymethyl chitosan nano-particles functionalized with ethylenediamine. J Radioanal Nucl Chem 308(3):935–946
91. Pan N, Li L, Ding J, Li S, Wang R, Jin Y, Wang X, Xia C (2016) Preparation of graphene oxide-manganese dioxide for highly efficient adsorption and separation of Th(IV)/U(VI). J Hazard Mater 309:107–115
92. Abd El-Magied MO, Tolba AA, El-Gendy HS, Zaki SA, Atia AA (2017) Studies on the recovery of Th(IV) ions from nitric acid solutions using amino-magnetic glycidyl methacrylate resins and application to granite leach liquors. Hydrometallurgy 169:89–98
93. Dastbaz A, Keshtkar AR (2014) Adsorption of Th^{4+}, U^{6+}, Cd^{2+}, and Ni^{2+} from aqueous solution by a novel modified polyacrylonitrile composite nanofiber adsorbent prepared by electrospinning. Appl Surf Sci 293(28):336–344
94. Elabd AA, Abo-aly MM, Zidan WI, Bakier E, Attia MS (2013) Modified Amberlite IR120 by magnetic nano iron-oxide for uranium removal. Anal Chem Lett 3(1):46–64